ENTRANCE AND EXIT REGION FRICTION FACTOR MODELS FOR ANNULAR SEAL ANALYSIS

by

DAVID ALAN ELROD

August 1988

TL-SEAL-5-88

Turbomachinery Laboratory
Mechanical Engineering Department

Texas A&M University

College Station, Texas 77843-3123

ENTRANCE AND EXIT REGION FRICTION FACTOR MODELS FOR ANNULAR SEAL ANALYSIS

A Dissertation

by

DAVID ALAN ELROD

Submitted to the Graduate College of
Texas A&M University
in partial fulfillment of the requirements for the degree of

DOCTOR OF PHILOSOPHY

August 1988

Major subject: Mechanical Engineering

ABSTRACT

Entrance and Exit Region Friction Factor Models

For Annular Seal Analysis. (August 1988)

David Alan Elrod, B.S., Louisiana State University;

M.S., Texas A&M University

Co-Chairs of Advisory Committee: Dr. Dara Childs
Dr. Clayton Nelson

The Mach number definition and boundary conditions in Nelson's nominally-centered, annular gas seal analysis are revised. A method is described for determining the wall shear stress characteristics of an annular gas seal experimentally. Two friction factor models are developed for annular seal analysis: one model is based on flat-plate flow theory; the other uses empirical entrance and exit region friction factors. The friction factor predictions of the models are compared to experimental results. Each friction model is used in an annular gas seal analysis. The seal characteristics predicted by the two seal analyses are compared to experimental results and to the predictions of Nelson's analysis. The comparisons are for smooth-rotor seals with smooth- and honeycomb-stators. The comparisons show that the analysis which uses empirical entrance and exit region shear stress models predicts the static and stability characteristics of annular gas seals better than the other analyses. The analyses predict direct stiffness poorly.

ACKNOWLEDGEMENT

This project was supported by NASA Grant NAG3-181 from NASA Lewis Research Center.

TABLE OF CONTENTS

Page

LIST OF TABLES

LIST OF FIGURES

Page

NOMENCLATURE

C, c	Direct and cross-coupled damping coefficients (FT/L)
D	Diameter (L)
D_e	Effective seal diameter, introduced in equation (22) (L)
d_c	Honeycomb cell size, illustrated in figure 5 (L)
e	Surface roughness (L)
F	Seal reaction-force magnitude (F)
f	Fanning friction factor
H	Radial clearance (L)
h_c	Honeycomb cell depth, illustrated in figure 5 (L)
K, k	Direct and cross-coupled stiffness coefficients (F/L)
L	Seal length (L)
L_e	Entrance length (L)
no, mo	Friction coefficients
Pr	Seal inlet-to-exit pressure ratio (dimensionless)
p	Fluid pressure (F/L^2)
R	Seal radius (L)
R_e	Nominal duct-flow Reynolds number $(1.33\rho UH/\mu)$
R_x	Flow-distance Reynolds number $(\rho Ux/\mu)$
U	Fluid bulk flow velocity (L/T)
u	Dimensionless bulk flow velocity, $U/R\omega$
X, Y	Rotor to stator relative displacement components (L)
x	Flow distance (L)
z	Axial location within the seal (L)

γ	Ratio of specific heats for air
κ	Entrance loss coefficient
μ	Fluid viscosity (FT/L^2)
ρ	Fluid density (M/L^3)
τ_w	Wall shear stress (F/L^2)
Ψ	Empirical friction multiplier, introduced in Chapter VI (dimensionless)
ω	Shaft angular velocity $(1/T)$

Subscripts

a	Reservoir value
b	Sump value
d	Developing flow region
r	Rotor
s	Stator
x	Exit region
z	Axial
θ	Circumferential
0, 1	Zeroth- and first-order values

CHAPTER I

INTRODUCTION

In pumps, compressors, turbines, and other turbomachines, annular seals are provided to limit the leakage between regions at different pressures. However, the forces within a seal may also influence rotordynamic response. In rotordynamics, a gas seal is modeled as a set of springs and dampers between the rotating shaft, or rotor, and the non-rotating housing, or stator. The model used to define the reaction–force/motion relationship for a nominally centered gas seal is

$$-\begin{Bmatrix} F_X \\ F_Y \end{Bmatrix} = \begin{bmatrix} K & k \\ -k & K \end{bmatrix} \begin{Bmatrix} X \\ Y \end{Bmatrix} + \begin{bmatrix} C & c \\ -c & C \end{bmatrix} \begin{Bmatrix} \dot{X} \\ \dot{Y} \end{Bmatrix}. \tag{1}$$

In this equation, X and Y are the displacement components of the rotor relative to the stator, and F_X and F_Y are the components of the reaction force acting on the rotor. The direct stiffness K, cross-coupled stiffness k, direct damping C, and cross-coupled damping c are referred to collectively as rotordynamic coefficients. The cross-coupled terms account for the fact that motion in one direction causes a force in an orthogonal direction.

Figure 1 shows the forces on a rotor in a forward circular orbit of amplitude A and frequency ω. Positive direct stiffness and cross-coupled damping act to center the rotor. Positive direct damping acts opposite to the velocity direction, opposing the whirling motion. However, positive cross-coupled stiffness acts to support the whirling motion–a destabilizing effect. Cross-coupled stiffness depends on the magnitude and direction (with respect to rotor rotation) of the circumferential velocity of the fluid within the seal.

Journal Model: ASME Journal of Tribology

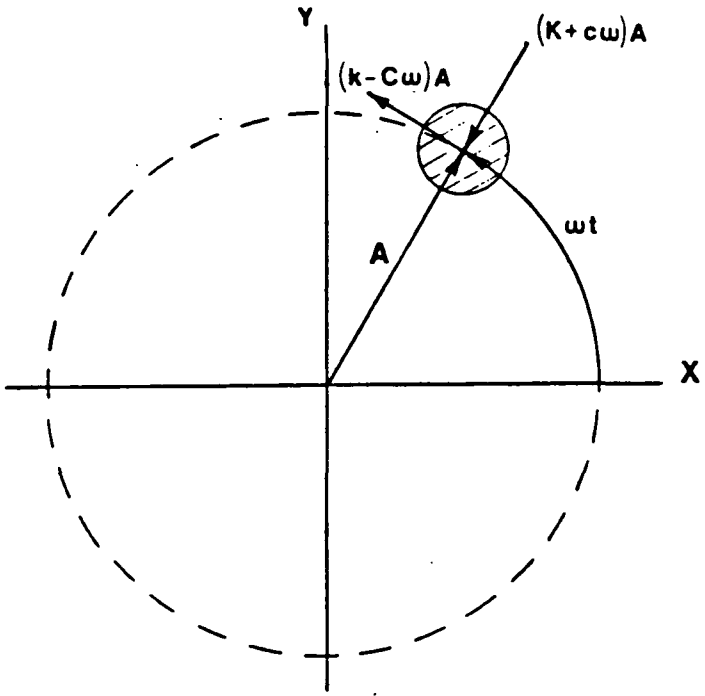

Figure 1. Forces on a precessing seal rotor.

Since Lomakin (1958) first demonstrated that the stiffness of an annular, liquid seal can cause an increase in the critical speed of a rotor, a number of analyses have been developed to predict the rotordynamic coefficients of incompressible and compressible annular seals. For incompressible seals, Black and Jenssen (1969, 1970) use a bulk-flow analysis in which the circumferential bulk-flow velocity is assumed to be one half of the rotor surface speed and the wall shear stresses are defined by average circumferential and axial Reynolds numbers. Their "short-seal" solution neglects the effect of pressure perturbations on circumferential flow. In another analysis, Black and Jenssen (1971) define wall shear stresses as a function of the local Reynolds numbers. Allaire et al. (1976) use Black's model for small rotor motion about a centered position to numerically calculate dynamic coefficients for motion about an eccentric position. Black et al.

(1981) account for the influence of inlet swirl, demonstrating that the circumferential bulk-flow velocity of a fluid element approaches one half of the rotor surface speed as it proceeds axially through the seal. Von Pragenau (1982) proposed a "damper seal" configuration, using a smooth rotor with a rough-surface stator, to reduce the fluid circumferential velocity and destabilizing cross-coupled stiffness of the seal. Childs' (1983, 1984) incompressible seal analyses provide "finite-length" solutions for constant-clearance and tapered seals, in which the effect of pressure perturbations on the circumferential bulk-flow velocity are included. Childs and Kim (1985) have developed a finite-length solution for incompressible seals with different surface roughness conditions on the rotor and stator, the damper-seal configuration proposed by von Pragenau. Dietzen and Nordmann (1986) use finite-difference methods and a three-dimensional fluid flow model to calculate seal rotordynamic coefficients. Their analysis has been used for grooved and smooth-surface seals.

Compressible flow in annular seals has been analyzed by Fleming (1978, 1980), Nelson (1984, 1985), and Nordmann et al. (1987). Fleming presents a short-seal solution for the leakage, direct stiffness, and direct damping of straight and tapered, smooth, annular gas seals. However, since he assumes one-dimensional, axial flow, Fleming cannot predict the cross-coupled coefficients. In his finite length analyses, Nelson accounts for the influence of inlet swirl and provides for shear and pressure effects on the circumferential bulk-flow velocity in constant-clearance or convergent-tapered gas seals with different rotor and stator surface roughnesses. In Chapter II, Nelson's analysis is reviewed, and his Mach number definition and boundary conditions are revised. The revised analysis is referred to as the fully-developed-flow analysis in the present study. Nordmann et al. (1987) extend the finite-difference, incompressible seal analysis of Dietzen and

Nordmann (1986) to calculate rotordynamic coefficients for annular gas seals. For a honeycomb-stator seal, the stator-wall boundary conditions assumed by Nordmann et al. would not apply.

For a given set of seal operating conditions, each of the above analyses predicts a pressure profile within the seal, which is integrated to determine forces and rotordynamic coefficients. Each analysis uses an abrupt loss at the seal entrance to model the high friction in the "developing flow region" of the seal. Actually, the developing flow region is often a substantial portion of the seal length. In Chapter III, an improved model for friction in the entrance region of a seal is developed from flat plate flow theory. The flat-plate-flow friction model is used in a gas seal analysis (called the flat-plate-flow analysis), described in Chapter III. In Chapter V, the friction factor predictions of the flat-plate-flow model are compared to experimental friction factors obtained using the test apparatus described in Chapter IV. In Chapter VI, experimental friction factor data are used to develop an empirical friction factor model for an annular gas seal analysis (the empirical-friction-factor analysis). In Chapters VII and VIII, static and dynamic results from experimental tests of four annular seals are compared to the predictions of the fully-developed-flow, flat-plate-flow, and empirical-friction-factor analyses.

CHAPTER II

NELSON'S ANALYSIS: A FULLY-DEVELOPED-FLOW MODEL

Nelson's analyses (1984,1985) predict both static and dynamic characteristics for nominally-centered, annular gas seals. The static results include fluid leakage through the seal, pressure gradient along the seal axis, and the fluid axial and circumferential velocities through the seal. Dynamic data provided by the analyses consist of the rotordynamic coefficients (direct and cross-coupled stiffness and damping terms) in equation (1).

In his analyses, Nelson uses a modified Hirs' (1973) turbulent bulk-flow fluid model to develop governing axial and circumferential momentum equations, and his model is completed by the continuity and energy equations. The equations define the relationship between the clearance, pressure, density, axial velocity, and circumferential velocity (H, p, ρ, U_z, and U_θ) as functions of the spatial variables θ and z and time t. Hirs' model uses the Blasius shear stress formula for fully-developed turbulent pipe flow, in which the friction factor f is

$$f = no R_e^{mo} \ , \tag{2}$$

R_e is the Reynolds number relative to the surface upon which the shear stress is acting, and the constants no and mo are generally determined empirically from static pressure flow experiments. In a bulk-flow analysis for incompressible seals, Nelson and Nguyen (1987) use Moody's pipe friction formula (Massey, 1979) instead of equation (2). Previously used in seal analysis by von Pragenau (1982), this formula approximates duct friction as presented in the Moody chart:

$$f = 0.001375 \left[1 + \left(20000 \frac{e}{D} + \frac{10^6}{R_e} \right)^{1/3} \right] \tag{3}$$

where e is the surface roughness ("bump" height) of the duct, D is the effective diameter of the duct, and R_e is the Reynolds number relative to the surface upon which the shear stress is acting.

Assuming small motion of the rotor about a centered position, Nelson uses a perturbation analysis similar to that employed by Childs (1983) to develop zeroth and first-order perturbation equations. The governing equations are expanded in the perturbation variables

$$\begin{aligned} H &= H_0 + \epsilon H_1 \qquad p = p_0 + \epsilon p_1 \qquad \rho = \rho_0 + \epsilon \rho_1 \\ U_z &= U_{z0} + \epsilon U_{z1} \qquad U_\theta = U_{\theta 0} + \epsilon U_{\theta 1}. \end{aligned} \tag{4}$$

The zeroth-order solution represents a zero-eccentricity flow condition, with rotor rotation but without precession. This solution is developed iteratively and yields the mass-leakage flow rate, and the axial distributions of pressure, density, axial velocity, and circumferential velocity. The iterative solution scheme uses initial guesses for the zeroth-order seal entrance Mach number and entrance pressure-loss coefficient. The entrance-loss relationship is defined by

$$\overline{p}_0(0) = \left[1 + \frac{(\gamma - 1)\,(\kappa + 1)\,M_0^2(0)}{2}\right]^{\gamma/(1-\gamma)} \tag{5}$$

where $\overline{p}_0(0)$ is the ratio of the seal entrance pressure to the reservoir stagnation pressure and $M_0(0)$ is the entrance Mach number. The entrance Mach number is iteratively adusted, and the loss coefficient κ is recalculated according to the relationship

$$\kappa = \sqrt{\frac{5.3}{\log_{10} R_e}} - 1.0 \ . \tag{6}$$

κ is used to model the high friction predicted by Deissler (1953) in the developing flow region of a duct. The iterative solution procedure for $M_0(0)$ and κ continues until either:

1) the Mach number at the exit reaches unity and the exit pressure is greater than the sump pressure (choked flow), or

2) the exit pressure equals the sump pressure and the exit Mach number is less than unity (unchoked flow).

The pressure, density, and velocity distributions and their axial derivatives, which are determined in the zeroth-order solution, are used in defining coefficients of the first-order perturbation equations. These equations define the pressure, density, and axial and circumferential velocity perturbations (p_1, ρ_1, U_{z1}, and $U_{\theta 1}$) due to rotor motion. The four physical boundary conditions required for the solution of these equations depend on the perturbation conditions that are specified at the seal entrance and exit. Numerical integration of the governing ordinary differential equations in the perturbation variables provides the first-order solution. The first-order pressure solution is then integrated axially and circumferentially for the rotordynamic coefficients in equation (1). The seal boundary conditions used by Nelson (1984, 1985) have been changed for the fully-developed-flow, flat-plate-flow, and empirical-friction-factor analyses of the present study. A discussion of the changes follows.

In Nelson's analyses (1984, 1985), the zeroth-order circumferential velocity at the seal entrance (i.e. at $z = 0$) is equal to the reservoir circumferential velocity, and the entrance circumferential velocity perturbation is zero; i.e.,

$$U_{\theta 0}(0) = U_{\theta a} \qquad U_{\theta 1}(0) = 0 \ . \tag{7}$$

These boundary conditions have not been changed in the present analyses.

The Mach number definition in Nelson's analyses is

$$M^2 = \frac{U_z^2 \rho}{\gamma p} \ . \tag{8}$$

For choked flow, $M = 1$ at the seal exit. When Mach number is defined by equation (8), the fluid velocity exceeds the velocity of sound when $M = 1$ unless $U_\theta = 0$. In general, the circumferential component of the fluid velocity is not zero at the seal exit. In the present study, the Mach number in the seal is defined by

$$M^2 = \frac{(U_z^2 + U_\theta^2)\,\rho}{\gamma p} \ . \tag{9}$$

The fluid velocity equals the velocity of sound when $M = 1$ in equation (9). The first-order perturbation of the Mach number in equation (8) is

$$M_1 = M_0 \left(\frac{\rho_1}{2\rho_0} + \frac{U_{z1}}{U_{z0}} - \frac{p_1}{2p_0} \right) \ . \tag{10}$$

For choked flow, M_1 is zero at the seal exit ($z = L$). In Nelson's analyses, this yields

$$\frac{\rho_1(L)}{2\rho_0(L)} + \frac{U_{z1}(L)}{U_{z0}(L)} - \frac{p_1(L)}{2p_0(L)} = 0 \ . \tag{11}$$

Using the Mach number definition of equation (9), equation (11) is replaced by

$$\frac{\rho_1(L)}{2\rho_0(L)} + \frac{U_{z0}(L)U_{z1}(L) + U_{\theta 0}(L)U_{\theta 1}(L)}{U_{z0}^2(L) + U_{\theta 0}^2(L)} - \frac{p_1(L)}{2p_0(L)} = 0 \ . \tag{12}$$

For unchoked flow, the first-order perturbation in the exit pressure is zero:

$$p_1(L) = 0 \ . \tag{13}$$

An expansion of equation (5) in the perturbation pressure and perturbation Mach number (equation (10)) yields a first-order pressure loss equation which must be satisfied at the seal entrance in Nelson's first-order solution:

$$p_1(0) + \frac{r p_0(0)}{2p_0(0) - r} \left(\frac{\rho_1(0)}{\rho_0(0)} + \frac{2U_{z1}(0)}{U_{z0}(0)} \right) = 0 \ , \tag{14}$$

where

$$r = \frac{\gamma\,(\kappa + 1)\,p_0(0) M_0^2(0)}{1 + (\gamma - 1)\,(\kappa + 1)\,\dfrac{M_0^2(0)}{2}} \ . \tag{15}$$

In the present analyses, equation (14) is replaced by

$$p_1(0) + \frac{r p_0(0)}{2p_0(0) - r}\left(\frac{\rho_1(0)}{\rho_0(0)} + \frac{2U_{z0}(0)U_{z1}(0)}{U_{z0}^2(0) + U_{\theta 0}^2(0)}\right) = 0 \ , \tag{16}$$

which is the first-order expansion of equation (5) using equation (9), with $U_{\theta 1}(0) = 0$.

The final first-order boundary condition in Nelson's analyses is derived from an expression for the density at the seal entrance:

$$\overline{\rho}_0(0) = \overline{p}_0(0)\left(1 + \frac{\gamma - 1}{2} M_0^2(0)\right) \ . \tag{17}$$

Expanding equation (17) in terms of the perturbation pressure, density, and Mach number (equation (10)), Nelson obtains

$$\overline{\rho}_1(0) + \frac{r s \overline{\rho}_0(0)}{2\overline{\rho}_0(0) + rs}\left(\frac{2U_{z1}(0)}{U_{z0}(0)} - \frac{\overline{p}_1(0)}{\overline{p}_0(0)}\right) = 0 \ , \tag{18}$$

where

$$s = 1 + (\gamma - 1)\frac{[M_0^2(0)(\kappa + 1) - 2]}{2\gamma(\kappa + 1)} \ , \tag{19}$$

and r is defined by equation (15). In the present analyses, use of the Mach number definition in equation (9) alters this boundary condition as follows:

$$\overline{p}_1(0) - \frac{\overline{p}_0(0)}{\overline{\rho}_0(0)}\overline{\rho}_1(0) + \frac{(\gamma - 1)\,\overline{\rho}_0(0)U_{z0}(0)}{\gamma} U_{z1}(0) = 0 \ . \tag{20}$$

In the present study, the boundary conditions in equations (7), (12), (16), and (20) are used in the fully-developed-flow, flat-plate-flow, and empirical-friction-factor analyses, with $\kappa = 0$ for the flat-plate-flow and empirical-friction-factor analyses.

CHAPTER III

A FLAT-PLATE-FLOW FRICTION FACTOR MODEL

The "developing flow" or "entrance" region of a seal is often a substantial portion of the seal length. However, in seal analyses, an entrance-loss coefficient (e.g. κ in equations (5) and (6)) is generally used to model the high losses in the developing flow region as abrupt losses at the seal inlet, and fully developed flow is assumed throughout the seal. In this chapter, a friction factor model is developed for the entrance region of an annular seal as the following questions are answered:

1) In duct flow, what are the developing flow and fully developed flow regions?

2) How does fluid friction in the developing flow region differ from fluid friction in the fully developed flow region?

3) In the flat-plate-flow seal analysis, how does the friction model in the developing flow region differ from that of the fully-developed-flow analysis?

As fluid enters a duct, a viscous boundary layer is formed along the duct wall (figure 2). At the wall, the fluid velocity is zero. Viscous effects cause a reduction of the velocity of adjacent fluid particles. At the center of the duct, a "free stream" region exists where the wall shear has not yet caused a reduction in fluid velocity. The region between the free-stream core and the duct wall is the boundary layer. The boundary layer becomes thicker as the fluid flows through the duct, and the free stream accelerates, satisfying the conservation of mass requirement. In figure 2, a plot of the velocity u versus the radial location r at a given z is called the

velocity profile at z. If the duct is long enough, the boundary layer will extend to the center of the duct, and at some finite distance L_e (the "entrance length") from the duct entrance, the velocity profile will cease to change with increasing z. When the velocity profile ceases to change, the flow is said to be fully developed. The entrance or developing flow region extends from the duct inlet to the fully developed flow region.

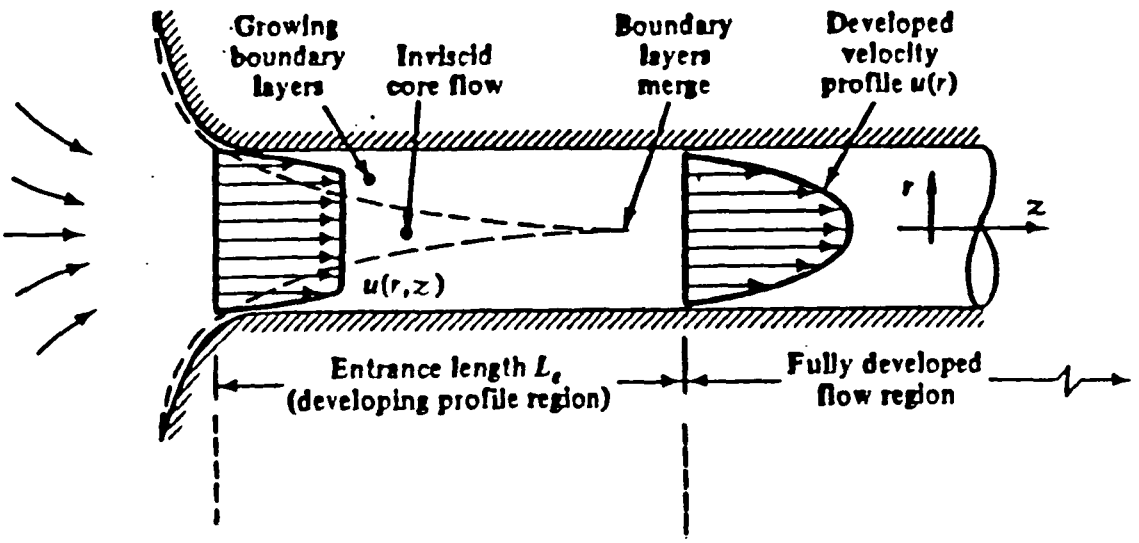

Figure 2. Developing flow in a duct.

Fluid friction models for the fully developed flow region are numerous (see Serghides, 1984). The accuracy of a model is generally evaluated by comparing the friction factor (f) predicted by the model to friction data plotted in the Moody diagram. The relationship between friction factor f and wall shear stress τ_w is:

$$f = \frac{\tau_w}{0.5\rho U^2} \cdot \tag{21}$$

In their seal analyses, Nelson (1984) and Nelson and Nguyen (1987) use two fully developed flow friction models: Moody's equation, which approximates the Moody

diagram well for Reynolds numbers between 4000 and 10^7 and relative roughnesses (e/D) up to 0.01, and Blasius' equation. For a given pipe Reynolds number, Blasius' model can be used to approximate both the Moody diagram friction factor f and the effect of small changes in Reynolds number on f. In general, however, the friction coefficient values *no* and *mo* which must be used to approximate the Moody diagram depend on Reynolds number and relative roughness. In the friction factor model developed in this Chapter, Moody's equation is used for the fully-developed-flow friction factor when the relative roughness is less than 0.01 ("smooth" surfaces) and Blasius' model is used for honeycomb surfaces.

Deissler (1953), Shapiro and Smith (1948), and Keenan and Neumann (1946) are among those who have investigated fluid friction in duct entrance regions. In an analysis of turbulent flow in the entrance regions of smooth passages, Deissler (1953) extends a previous analysis for fully developed, turbulent flow. Figures 3 and 4 (from Deissler, 1953) show the friction factors Deissler predicts for flow through a tube and for flow between parallel plates, respectively. In each plot, X/D is the flow distance in hydraulic diameters. Deissler predicts that the friction factor reaches its fully developed flow value in about 10 diameters. In his annular seal analysis, Nelson (1984) uses a fully developed flow friction factor throughout the seal, modeling the excess losses predicted by Deissler in the entrance region as abrupt losses at the seal inlet.

In an experimental study in the 1940's, Shapiro and Smith (1948) determined friction factors in the entrance region of smooth, round tubes with bellmouth entries for uniform inlet conditions. Shapiro and Smith used water and air at low Mach numbers as test fluids, at Reynolds numbers (based on tube diameter) from 39,000 to 590,000. The diameters of the test pipes ranged from 9.5 to 102 mm. Their study shows that, for developing duct flow, the Reynolds number based on

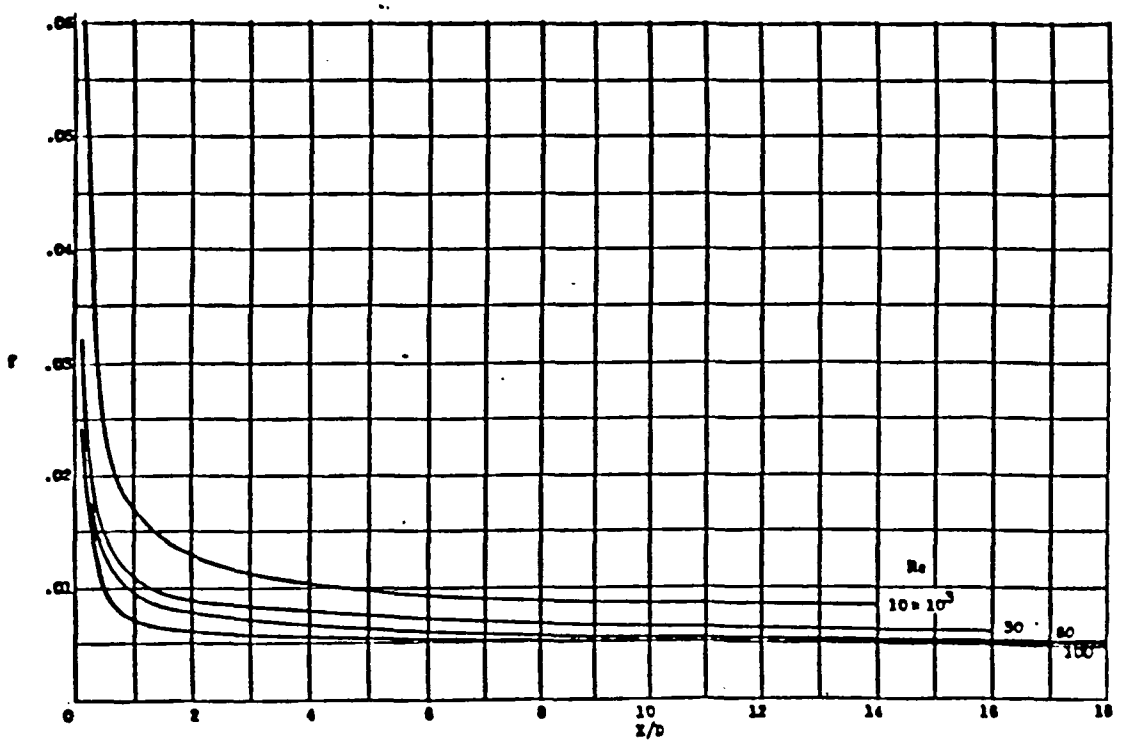

Figure 3. Variation of friction factor in the inlet region of a tube (from Deissler, 1953).

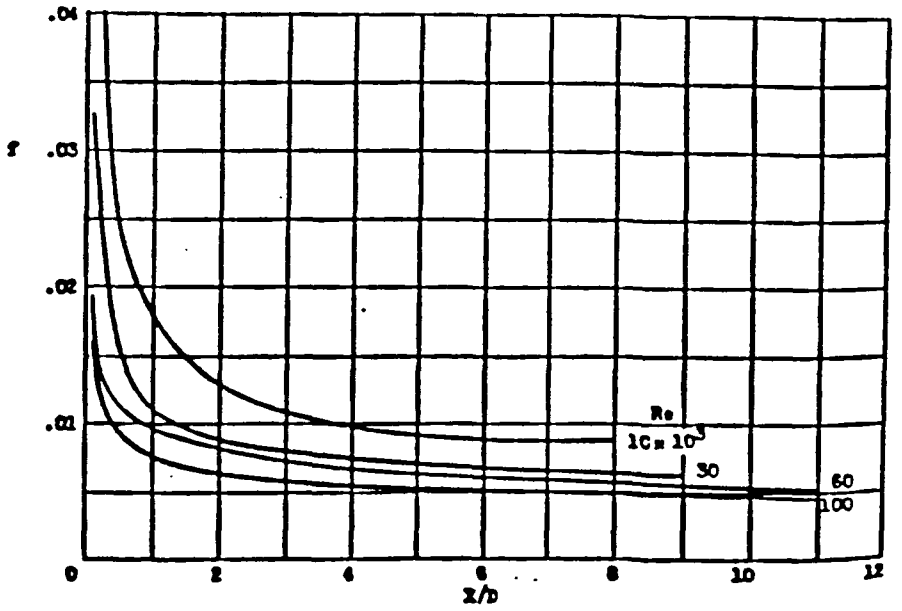

Figure 4. Variation of friction factor in the inlet region between two flat parallel plates (from Deissler, 1953).

distance from the inlet is more significant in predicting friction factors than the pipe (diameter-based) Reynolds number. The friction factor is within 5% of the fully developed flow value "beginning at about 40 to 60 tube diameters from the tube inlet." Furthermore, Shapiro and Smith predict that the friction factor is "almost infinite" at the tube inlet. Boundary layer characteristics in the entrance region of a tube are similar to boundary layer characteristics in flat plate flow studies.

In another experimental study, Keenan and Neumann (1946) report friction factors for subsonic air flow at Reynolds numbers from 100,000 to 450,000. The test pipe was a piece of standard drawn-brass tubing with an inside diameter of 9.5 mm. The study shows that the friction factor decreases from a high value near the tube inlet to the fully developed flow value at a flow distance of about 40 pipe diameters.

For friction-factor calculations, the effective diameter of an annular seal is four-thirds of the seal radial clearance (White, 1979); i.e.,

$$D_e = \frac{4}{3}H \quad . \tag{22}$$

Based on the data described in the preceding paragraph, fully developed friction factor values may not be attained for a substantial portion of the seal length. For example, forty diameters is over 60% of the length of the turbine interstage seal of the High-Pressure Oxidizer Turbopump of the Space Shuttle Main Engine (described by Nelson, 1984). Previous seal analyses (and the fully-developed-flow analysis of the present study) use fully-developed-flow friction models, which are a function of duct diameter, throughout the seal. The only exception is the analysis of Mullins and Barrett (1983), which uses an entrance region friction factor model. However, the friction factor is assumed to increase from zero at

the seal inlet to the fully-developed-flow friction value at the end of the entrance region, which disagrees with the results described in the previous paragraphs and shown in figures 3 and 4. Furthermore, the entrance region friction factor used by Mullins and Barrett depends on the effective diameter of the seal and on the axial component of the flow distance. In the following paragraphs, a new friction factor model for the entrance region of a duct is developed. In this model, friction is not a function of duct diameter; it is a function of the total flow distance within the seal (axial and circumferential components).

Fluid friction in the entrance region of a duct has been compared to fluid friction along a flat plate. For flat plate flow (zero pressure gradient by definition), f depends on distance from the leading edge of the plate. A number of equations have been used to model f for turbulent flow past a flat plate, and a common functional form is

$$f = aR_x^b \ , \tag{23}$$

where x is the distance from the leading edge and R_x is the Reynolds number defined by:

$$R_x = \frac{\rho U x}{\mu} \ . \tag{24}$$

If a pressure gradient is present (i.e. $dp/dx \neq 0$), f is determined by numerical analysis. According to White (1974), there are few analyses for compressible, turbulent flow with a non-zero pressure gradient over a flat plate. Available solution methods require knowledge of the free-stream velocity gradient and empirical boundary layer relationships. The use of one of these plate-flow numerical solution methods (an external flow analysis) for entrance flow in a duct (an internal flow problem) is questionable since boundary layer interaction in a duct complicates the flow.

In the flat-plate-flow analysis of the present study, Nelson's (1984, 1985) governing equations are used, and the solution method is the same as for the fully-developed-flow model. In the flat-plate-flow analysis, the friction factor in the developing flow region of an annular seal is modeled by equations (23) and (24), where x is a flow distance relative to the rotor or stator surface. For calculating the wall shear stress at the seal stator in the developing flow region, the friction factor for the zeroth-order solution is

$$f_{s0} = a_s \left(\frac{\rho_0 x_s}{\mu} \right)^{b_s} (U_{\theta 0}^2 + U_{z0}^2)^{(b_s/2)} \quad . \tag{25}$$

For the shear stress at the rotor, the friction factor is

$$f_{r0} = a_r \left(\frac{\rho_0 x_r}{\mu} \right)^{b_r} [(U_{\theta 0} - R\omega)^2 + U_{z0}^2]^{(b_r/2)} \quad . \tag{26}$$

The equations for flow distance relative to the stator and rotor (x_s and x_r, respectively) at an axial location Z are

$$x_s(Z) = \int_0^Z \left[1 + \left(\frac{U_{\theta 0}}{U_{z0}} \right)^2 \right]^{1/2} dz \tag{27}$$

$$x_r(Z) = \int_0^Z \left[1 + \left(\frac{U_{\theta 0} - R\omega}{U_{z0}} \right)^2 \right]^{1/2} dz \quad . \tag{28}$$

The coefficient a and the exponent b in equation (23) are calculated by setting the developing-flow friction factor f_d equal to the fully-developed-flow friction factor f_f at a flow distance of forty diameters; i.e.,

$$f_{d(x=40D_e)} = a \left[\frac{\rho U (40 D_e)}{\mu} \right]^b = a(40R_e)^b = f_f \quad . \tag{29}$$

When Moody's equation (equation (3)) is used for f_f, a and b values are calculated by solving the following equations:

$$f_f = a(40R_e)^b = 0.001375 \left[1 + \left(20000 \frac{e}{1.33 H_0} + \frac{10^6}{R_e} \right)^{1/3} \right] \tag{30}$$

and

$$\frac{\partial f_f}{\partial R_e} = \frac{ab}{R_e}(40R_e)^b = -\frac{1375}{3R_e^2}\left(20000\frac{e}{1.33H_0} + \frac{10^6}{R_e}\right)^{-2/3} . \tag{31}$$

For any iteration in the zeroth-order solution (described in Chapter II), only a and b are unknown in equations (30) and (31). Equations (30) and (31) are used to calculate a set of coefficients for both the rotor and the stator (i.e. a_r, b_r and a_s, b_s).

The expansion of equations (25) and (26) in terms of the perturbation variables in equation (4) yields

$$f_{s1} = f_{s0}b_s\left[\frac{\rho_1}{\rho_0} + \frac{x_{s1}}{x_{s0}} + \frac{U_{\theta 0}U_{\theta 1} + U_{z0}U_{z1}}{U_{\theta 0}^2 + U_{z0}^2}\right] \tag{32}$$

$$f_{r1} = f_{r0}b_r\left[\frac{\rho_1}{\rho_0} + \frac{x_{r1}}{x_{r0}} + \frac{(U_{\theta 0} - R\omega)U_{\theta 1} + U_{z0}U_{z1}}{(U_{\theta 0} - R\omega)^2 + U_{z0}^2}\right], \tag{33}$$

which are required for the first-order solution in the flat-plate-flow analysis. In equations (32) and (33),

$$x_{s1} = \frac{\partial x_s}{\partial U_{\theta 0}}U_{\theta 1} + \frac{\partial x_s}{\partial U_{z0}}U_{z1} \tag{34}$$

$$x_{r1} = \frac{\partial x_r}{\partial U_{\theta 0}}U_{\theta 1} + \frac{\partial x_r}{\partial U_{z0}}U_{z1} . \tag{35}$$

Using Leibnitz's rule and equation (27),

$$\frac{\partial x_s}{\partial U_{\theta 0}}(Z) = \int_0^Z \frac{U_{\theta 0}}{U_{z0}^2}\left[1 + \left(\frac{U_{\theta 0}}{U_{z0}}\right)^2\right]^{-1/2} dz . \tag{36}$$

Similar expressions can be derived for the other partial derivatives in equations (34) and (35). For the flat-plate-flow seal analysis, the following equations are numerically integrated in the zeroth-order solution for use in calculating the zeroth-

and first-order wall shear stresses in the seal:

$$\frac{\partial x_s}{\partial z} = \left[1 + \left(\frac{U_{\theta 0}}{U_{z0}}\right)^2\right]^{(1/2)} \tag{37}$$

$$\frac{\partial x_r}{\partial z} = \left[1 + \left(\frac{U_{\theta 0} - R\omega}{U_{z0}}\right)^2\right]^{(1/2)} \tag{38}$$

$$\frac{\partial(\partial x_s/\partial U_{\theta 0})}{\partial z} = \frac{U_{\theta 0}}{U_{z0}^2}\left[1 + \left(\frac{U_{\theta 0}}{U_{z0}}\right)^2\right]^{-1/2} \tag{39}$$

$$\frac{\partial(\partial x_s/\partial U_{z0})}{\partial z} = -\frac{U_{\theta 0}^2}{U_{z0}^3}\left[1 + \left(\frac{U_{\theta 0}}{U_{z0}}\right)^2\right]^{-1/2} \tag{40}$$

$$\frac{\partial(\partial x_r/\partial U_{\theta 0})}{\partial z} = \frac{U_{\theta 0} - R\omega}{U_{z0}^2}\left[1 + \left(\frac{U_{\theta 0} - R\omega}{U_{z0}}\right)^2\right]^{-1/2} \tag{41}$$

$$\frac{\partial(\partial x_r/\partial U_{z0})}{\partial z} = -\frac{(U_{\theta 0} - R\omega)^2}{U_{z0}^3}\left[1 + \left(\frac{U_{\theta 0} - R\omega}{U_{z0}}\right)^2\right]^{-1/2} \tag{42}$$

For a seal with a honeycomb stator, flow at the stator surface differs from the developing flow described above. In figure 5, the honeycomb cell size is d_c and the cell depth is h_c. The cell size and depth in a honeycomb-stator seal are usually from one to several times the seal clearance. The fluid velocity along the stator wall is not necessarily zero. Use of the three-dimensional seal analysis of Nordmann et al. (1987), which assumes "no-slip" boundary conditions at the stator, is questionable for a honeycomb seal. In the flat-plate-flow analysis, the developing-flow friction factor defined above is only used for shear stresses at the rotor for a honeycomb-stator/smooth-rotor seal. Throughout the seal, honeycomb-stator wall shear stresses are calculated using the Blasius friction factor:

$$f = noR_e^{mo} \ . \tag{2}$$

Chapter V includes comparisons of the friction factor predictions of the above model to experimental friction factors.

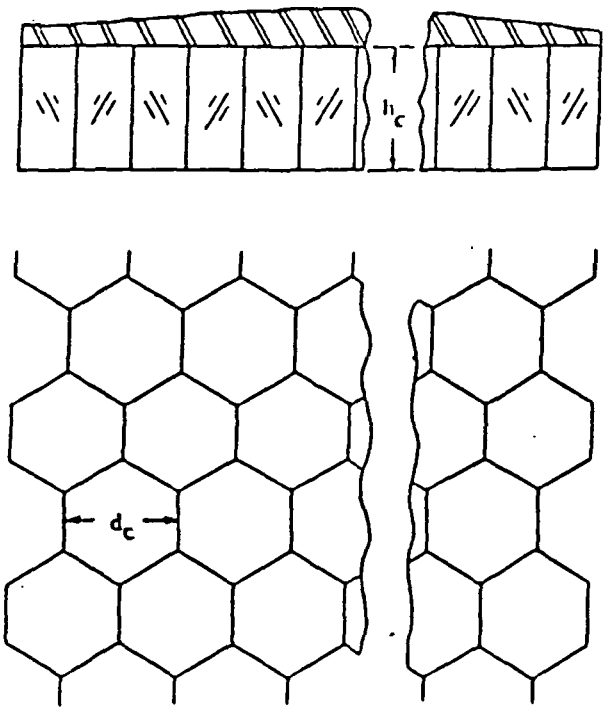

Figure 5. Honeycomb stator insert detail.

CHAPTER IV

TEST APPARATUS

A complete description of the test apparatus used in this study is provided by Childs et al. (1986 and 1988). The rotor shaft is suspended, pendulum fashion, from an upper, rigidly-mounted, pivot shaft, as illustrated in figure 6. This arrangement allows for a horizontal (harmonic) motion of the rotor. A cam within the pivot shaft allows vertical (static) positioning of the rotor. The rotor is excited, horizontally, by a hydraulic-shaker head which acts on the rotor-shaft housing. The design of the test rig, illustrated in figure 7, permits the installation of various rotor/stator combinations. The stator is supported in the test-section housing by three piezo-electric, quartz, load cells in a trihedral configuration.

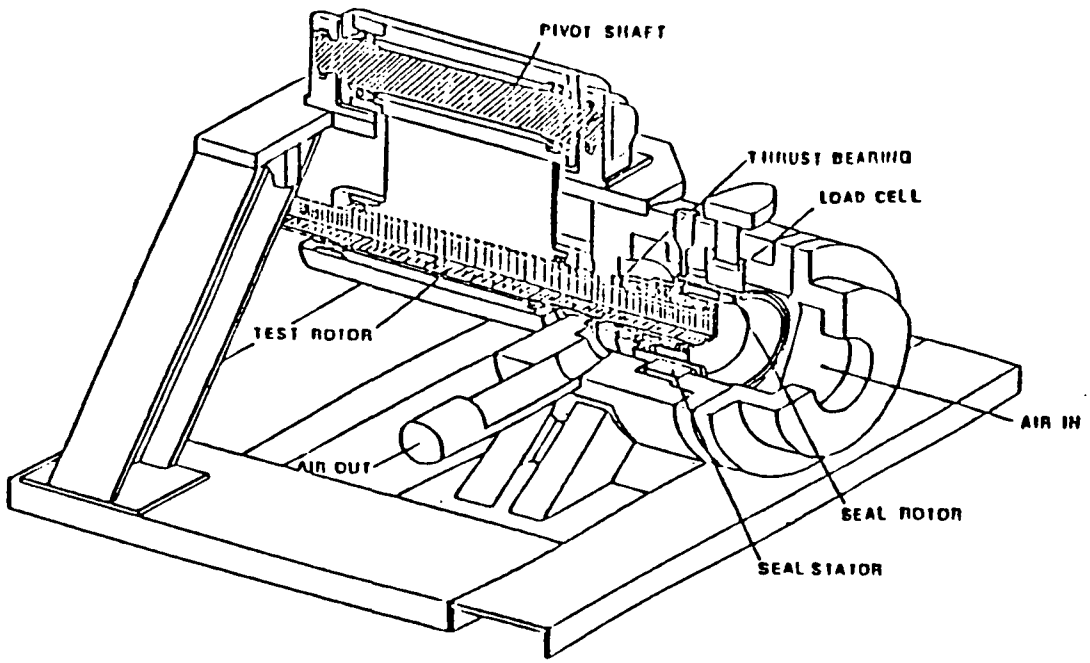

Figure 6. Test apparatus.

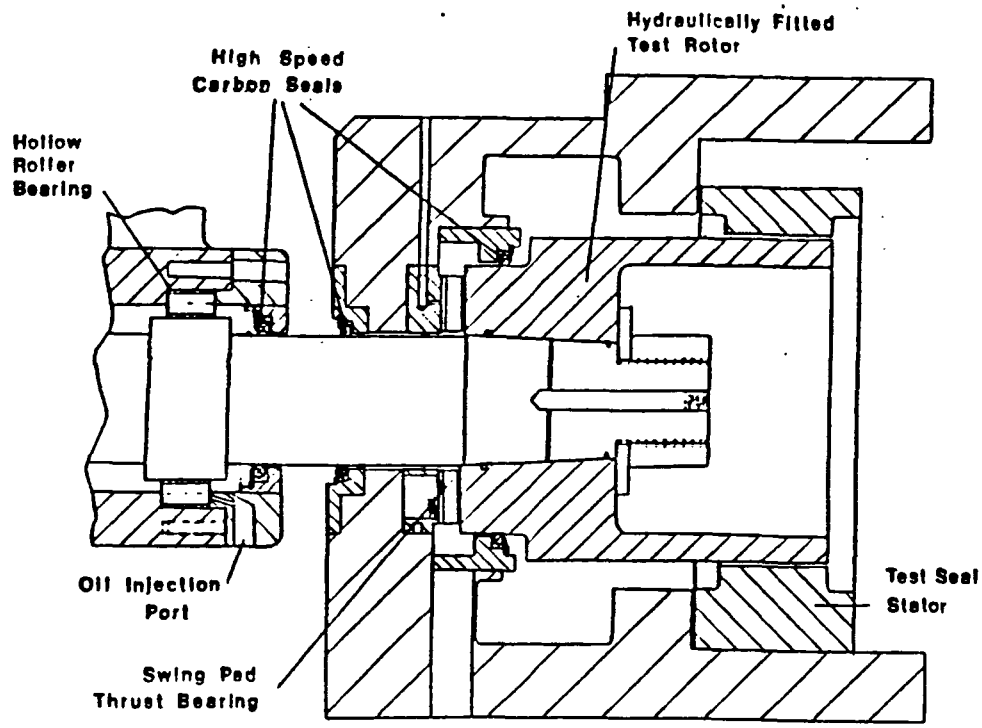

Figure 7. Test-section cross section.

For the present study, the test apparatus has been used to determine friction factors for the six seals listed in Table 1, and dynamic characteristics for seals S1, HC1, HC2, and HC3 of Table 1. In Table 1, seals S1, S2, and S3 are smooth-stator/smooth-rotor seals, and seals HC1, HC2, and HC3 are honeycomb-stator/smooth-rotor seals. In the honeycomb stator insert detail shown in figure 5, the honeycomb cell size is d_c and the cell depth is h_c. In Table 1, the cell sizes are 1.57 mm and 0.51 mm, and the cell depths are 1.91 mm and 1.47 mm. In all six seals, the diameter and measured surface roughness of the rotor were 151.4 mm and 0.188 μm, respectively.

The operator of the dynamic-seal-apparatus can control the following four independent variables: inlet pressure, rotor speed, shake frequency, and inlet

circumferential velocity. For dynamic tests, the actual test points for three of these variables are shown in Table 2. The sump pressure p_b was about 1.01 bars (atmospheric pressure). For all dynamic test results in the present study, the rotor was shaken about a centered position within the stator at a shake frequency of 74.6 Hz, and a shake amplitude of about 80 μm.

Table 1. Seal Dimensions

Seal	Length	Clearance, H	Stator Surface
S1	5.08 cm	0.41 mm	$e = 0.188\mu$m
S2	5.08 cm	0.30 mm	$e = 0.188\mu$m
S3	5.08 cm	0.20 mm	$e = 0.188\mu$m
HC1	5.08 cm	0.41 mm	1.57x1.91 mm cells
HC2	5.08 cm	0.41 mm	1.57x1.47 mm cells
HC3	5.08 cm	0.41 mm	0.51x1.47 mm cells

Table 2. Test Variables

Inlet Pressure	Rotor Speeds	Inlet Circumferential Velocities
1–3.08 bars	1– 3000 cpm	-2–High velocity against rotation
2–4.46 bars	2– 6000 cpm	-1–Low velocity against rotation
3–5.84 bars	3– 9500 cpm	0–Zero circumferential velocity
4–7.22 bars	4–13000 cpm	1–Low velocity with rotation
5–8.26 bars	5–16000 cpm	2–High velocity with rotation

The inlet circumferential velocity is controlled using four sets of inlet guide vanes. For the two "high" inlet circumferential velocity cases in Table 2, the guide-vane depth ("A" in figure 8) is 35% of the guide-vane depth for the "low" inlet circumferential velocity cases. The zero inlet circumferential velocity case is obtained without guide vanes. For a set of swirl vanes at a constant running speed, inlet circumferential velocity remains almost constant for the test pressure ratios in the table above. The velocity decreases slightly with rotor speed, mainly

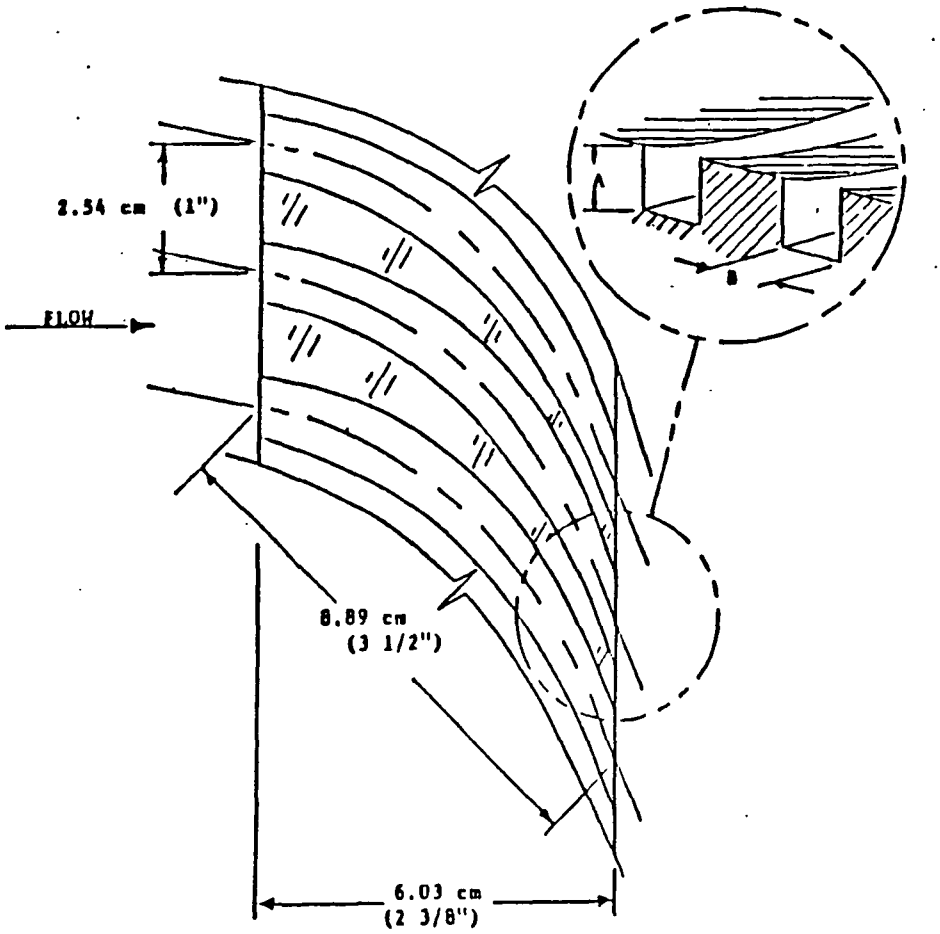

Figure 8. Inlet-guide-vane detail.

because the rotor grows with increasing speed and reduces the leakage. The ratio of inlet circumferential velocity to rotor surface velocity, $u_{\theta a}$, ranged from about -5 to about $+5$. Average experimental inlet circumferential velocities for seals S1, HC1, HC2, and HC3 are given in Table 3.

Table 3. Inlet Circumferential Velocities

Swirl	Smooth Seal	HC1	HC2	HC3
-2	-100 m/sec	-58 m/sec	-68 m/sec	-53 m/sec
-1	- 44 m/sec	-26 m/sec	-31 m/sec	-24 m/sec
0	0 m/sec	0 m/sec	0 m/sec	0 m/sec
1	45 m/sec	27 m/sec	31 m/sec	24 m/sec
2	118 m/sec	68 m/sec	80 m/sec	62 m/sec

CHAPTER V

EXPERIMENTAL FRICTION FACTORS

The test apparatus described in Chapter IV has been used to obtain friction factor data for the six seals listed in Table 1 of Chapter IV. In the present Chapter, the experimental method is described, and friction factor test results are compared to the predictions of the friction model used in the flat-plate-flow seal analysis.

Test Method

One-dimensional, steady, adiabatic flow of a perfect gas with constant specific heats through a constant-area duct with no external work is called Fanno line flow. The momentum equation for a control volume of length dz is

$$-A dp - \tau_w A_w = \rho A U dU \quad , \tag{43}$$

where A is the cross-sectional area of the duct, τ_w is the shear stress at the duct walls, and A_w is the surface area over which τ_w acts. For a seal with the rotor centered,

$$A = \frac{\pi}{4}(D_s^2 - D_r^2) \quad , \quad A_w = \pi(D_s + D_r)dz \quad , \quad \text{and} \quad D_s - D_r = 2H_0 \quad . \tag{44}$$

Substitution and simplification yields

$$-dp - \frac{2\tau_w}{H_0} dz = \rho U dU \quad . \tag{45}$$

The relationship between friction factor f and τ_w is expressed in equation (21):

$$f = \frac{\tau_w}{0.5\rho U^2} \quad . \tag{21}$$

Using equations (21) and (45), the perfect gas law, the definition of Mach number, and the conservation of mass requirement, one can derive (see John, 1984) that

the effective friction factor, f_e, for a seal is:

$$f_e = \frac{H}{M}\left[\frac{1-M^2}{\left(1+\frac{\gamma-1}{2}M^2\right)\gamma M^2}\right]\frac{dM}{dz} \quad . \tag{46}$$

To determine f_e for a seal using the test apparatus described in Chapter IV, the stator is mounted in the apparatus, a smooth rotor is centered in the stator, and flow tests are conducted. For each test, the rotor remains stationary (no rotation), the inlet air has no circumferential velocity component, and the seal inlet pressure is held constant. The stagnation temperature of the air, flow rate through the seal, and pressures along the seal length are measured. The Mach number is calculated at 3.2 cm (0.125 inch) intervals along the seal (i.e. at pressure tap locations). A least-squares cubic curve fit is used to express the Mach number as a function of axial location. Equation (46) is used to calculate f_e in the seal. Values of f_e have been calculated for three smooth-stator/smooth-rotor seals (S1, S2, and S3 in Table 1), and for three honeycomb-stator/smooth-rotor seals (HC1, HC2, and HC3 in Table 1).

For a seal with identical rotor and stator surfaces (i.e. a smooth-stator/smooth-rotor seal),

$$f_s = f_r = f_e \quad . \tag{47}$$

For a seal with different surface roughnesses (e.g. a honeycomb-stator/smooth-rotor seal), f_e, f_s, and f_r are related as follows. In equation (43),

$$\tau_w A_w = \tau_w (A_s + A_r) = \tau_s A_s + \tau_r A_r \quad , \tag{48}$$

and

$$A_r = \frac{D_r}{D_s} A_s \tag{49}$$

for a seal. Substitution from equation (21) and (49) into equation (48) yields

$$\frac{1}{2}\rho U^2 f_e \left(1+\frac{D_r}{D_s}\right) = \frac{1}{2}\rho U^2 \left(f_s + \frac{D_r}{D_s} f_r\right) \quad ,$$

or

$$f_e = \frac{1}{1 + \frac{D_r}{D_s}} \left(f_s + \frac{D_r}{D_s} f_r \right) \quad . \tag{50}$$

Rearranging,

$$f_s = \left(1 + \frac{D_r}{D_s} \right) f_e - \frac{D_r}{D_s} f_r \quad . \tag{51}$$

To determine the friction coefficients no_s and mo_s for a honeycomb stator, stationary-rotor tests are run, and f_s values are calculated for nine inlet pressures using equations (46) and (51). In equation (51), f_r is calculated using smooth-stator/smooth-rotor seal test results. When friction coefficients are calculated, entrance-region and end effects are avoided by using test data for axial locations from forty effective seal diameters to about 60% of the seal length. For each stator, average f_s results and average experimental Reynolds numbers in this region are used in a least-squares curve fit to determine mo_s and no_s (see equation (2)). The friction coefficients mo and no for the six seals listed in Table 1 are given in Table 4.

Table 4. Seal Friction Coefficients

Surface	no	mo
Smooth	0.154	-0.299
HC1 stator	0.303	-0.117
HC2 stator	0.155	-0.098
HC3 stator	0.424	-0.134

Experiment/Theory Comparisons

For the six seals of Table 1, typical plots of f_e versus dimensionless axial location (z/L) are shown in figure 9. For seal S2, the test case shown is for unchoked flow. For the other plots in figure 9, flow is choked. In each plot, experimental f_e results are designated by the letter "x". The error bands represent the uncertainty determined using the method described by Holman (1978). The

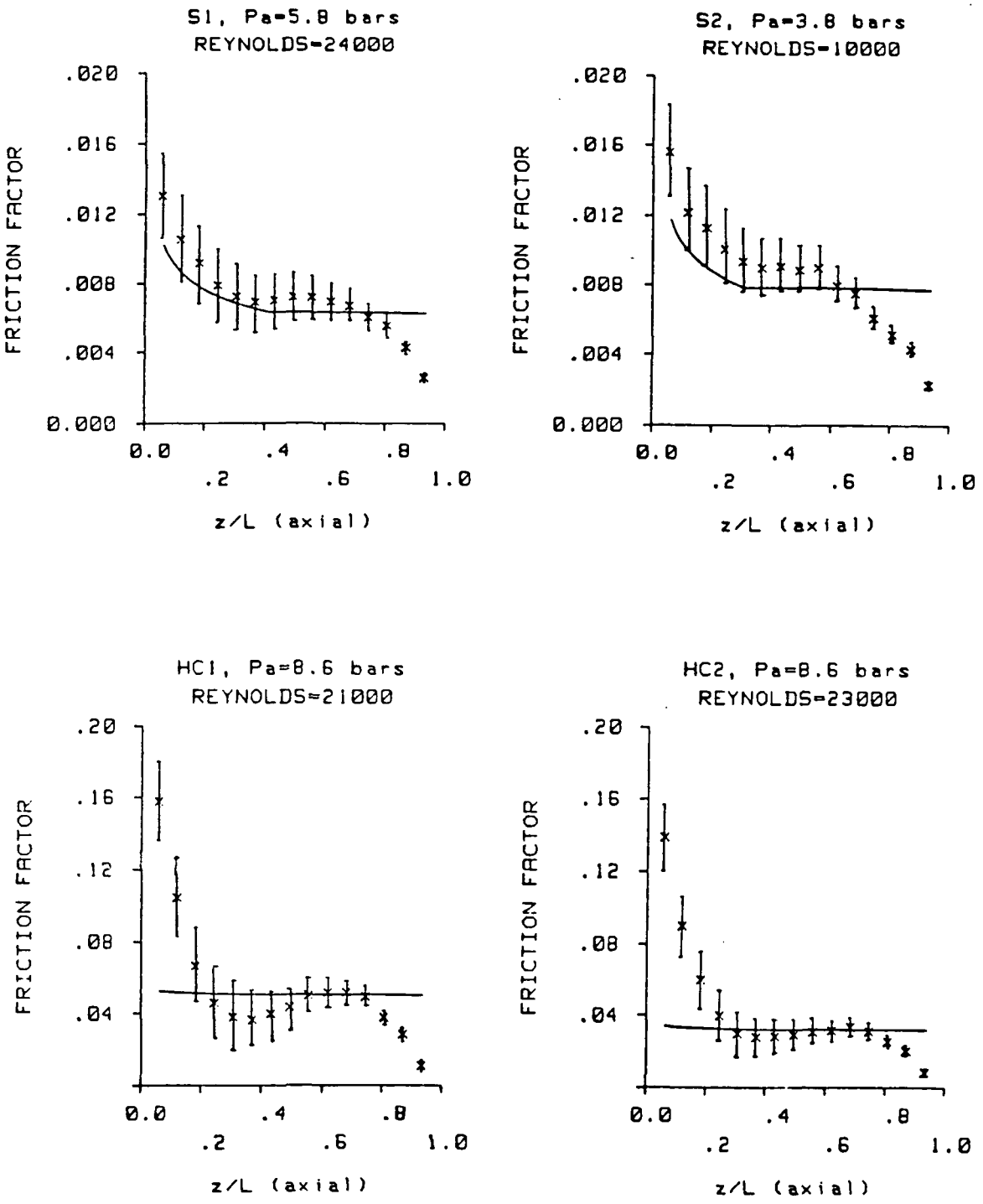

Figure 9. f_e **versus axial location for the seals in Table 1. Solid lines: predictions of the model in Chapter III.**

solid lines in the plots represent the friction factors predicted by the flat-plate-flow friction model and equations (47) and (50). For seal S1 of Table 1, $40D_e \approx 0.4L$. For seal S2, $40D_e \approx 0.3L$. In figure 9, the experimental friction factors for seals S1 and S2 are high and decreasing for about forty diameters. For the honeycomb-stator seals, f_e decreases in the first one-third of the seal, and then increases. For all six seals, the experimental friction factor is generally higher than predicted in the entrance region. In the middle 20% to 30% of seals S1 and S2, f_e is higher than predicted by Moody's equation. In the last 40% of all six seals of Table 1, f_e decreases experimentally. No existing friction factor model, including the flat-plate-flow friction model, predicts this decrease in f. In Chapter VI, a friction factor model is developed from experimental data obtained using the test apparatus described in Chapter IV.

CHAPTER VI

AN EMPIRICAL FRICTION FACTOR MODEL

Figure 9 in Chapter V shows that the friction factor in a seal decreases in the "exit" region of the seal. No existing friction factor model includes this feature. The high friction in the "entrance" region of the plots in figure 9 is underpredicted by the flat-plate-flow friction model. Furthermore, Moody's equation underpredicts the friction factor between the entrance and exit regions of the smooth-stator/smooth-rotor seals. In this chapter, a friction factor model based on the data in figure 9 is developed for annular seal analysis (the "empirical-friction-factor" seal analysis). The friction factor predictions of the model are compared to experimental data from stationary-rotor tests of the six seals of Table 1. In the empirical-friction-factor seal analysis, the friction model in this chapter is used in Nelson's (1984,1985) governing equations for a gas seal, and the solution method is the same as for the fully-developed-flow model.

For calculating the wall shear stress at the seal stator, the zeroth-order friction factor is

$$f_{s0} = \Psi_{ds0}\Psi_{x0}f_{Bs0} \ . \tag{52}$$

For the shear stress at the rotor, the friction factor is

$$f_{r0} = \Psi_{dr0}\Psi_{x0}f_{Br0} \ . \tag{53}$$

In equations (52) and (53), f_{Bs0} and f_{Br0} are the zeroth-order Blasius friction factors for the stator and rotor, respectively; i.e.,

$$f_{Bs0} = no_s \left(\frac{1.33\rho_0 H_0}{\mu}\right)^{mo_s} \left[U_{\theta 0}^2 + U_{x0}^2\right]^{mo_s/2} \tag{54}$$

$$f_{Br0} = no_r \left(\frac{1.33\rho_0 H_0}{\mu}\right)^{mo_r} \left[(U_{\theta 0} - R\omega)^2 + U_{x0}^2\right]^{mo_r/2} \tag{55}$$

The terms Ψ_{ds0}, Ψ_{dr0}, and Ψ_{x0} in equations (52) and (53) are defined in the following paragraphs.

Exit Region Friction

No existing friction model predicts a decrease in friction factor near the seal exit, as shown in figure 9. Others (e.g., Keenan and Neumann, 1946) have recognized that "end effects" are present in duct flow, but have chosen to avoid the region, experimentally. Figure 9 shows that the friction factor decreases to near zero as z/L increases from 0.6 to 1.0. In the empirical-friction-factor seal analysis, this region ($0.6 < z/L \leq 1.0$) is defined as the "exit region" of the seal, and Ψ_{x0} is used in equations (52) and (53) to model the friction factor decrease, where

$$\Psi_{x0} = -4.12 + 20.3(z/L) - 25.1(z/L)^2 + 9.03(z/L)^3 \ . \tag{56}$$

when $z/L > 0.6$. When $z/L \leq 0.6$, $\Psi_{x0} = 1.0$. The constant terms in equation (56) were obtained using the following friction factor data:

$$\frac{d\Psi_{x0}}{d(z/L)}(z/L = 0.60) = 0.00$$

$$\Psi_{x0}(z/L = 0.60) = 1.00$$

$$\Psi_{x0}(z/L = 0.80) = 0.72$$

$$\Psi_{x0}(z/L = 1.02) = 0.00$$

Entrance Region Friction - Smooth Surfaces

In equations (52) and (53), Ψ_{ds} and Ψ_{dr} are used to model the high friction in the developing flow region, where

$$\Psi_{ds} = 2.76 - 5.16(x_s/L_e) + 5.04(x_s/L_e)^2 - 1.64(x_s/L_e)^3 \tag{57}$$

and

$$\Psi_{dr} = 2.76 - 5.16(x_r/L_e) + 5.04(x_r/L_e)^2 - 1.64(x_r/L_e)^3 \ , \tag{58}$$

when $x/L_e < 1.0$, and

$$L_e = 40D_e = 53.33H \ . \tag{59}$$

For $x/L_e \geq 1.0, \Psi_d = 1.0$. The constants in equations (57) and (58) were obtained using the following friction factor data:

$$\frac{d\Psi_d}{d(x/L_e)}(x/L_e = 1.00) = 0.00$$

$$\Psi_d(x/L_e = 0.14) = 2.13$$

$$\Psi_d(x/L_e = 0.47) = 1.28$$

$$\Psi_d(x/L_e = 1.00) = 1.00$$

Figure 10 shows a comparison of typical experimental and predicted friction factors for the smooth-stator seals of Table 1. The model used for the predictions in figure 10 is defined by equations (52), (54), (56), and (57).

Honeycomb Stator Friction Factors

For all honeycomb-stator seals, equation (57), which is used in the calculation of smooth-stator friction factors, is replaced in the present empirical friction factor model by

$$\Psi_{ds} = 5.68 - 36.5(z/L) + 83.5(z/L)^2 - 58.4(z/L)^3 \tag{60}$$

for $z/L \leq 0.6$. For $z/L > 0.6$, $\Psi_{ds} = \Psi_{ds}(z/L = 0.6)$. The constants in equation (60) were obtained using the following friction factor data:

$$\frac{d\Psi_{ds}}{d(z/L)}(z/L = 0.60) = 0$$

$$\Psi_{ds}(z/L = 0.06) = 3.7$$

$$\Psi_{ds}(z/L = 0.33) = 0.63$$

$$\Psi_{ds}(z/L = 0.50) = 1.00$$

Figure 11 shows a comparison of experimental and predicted f_e for seals HC1, HC2, and HC3 of Table 1. The model used for the predictions in figure 11 is

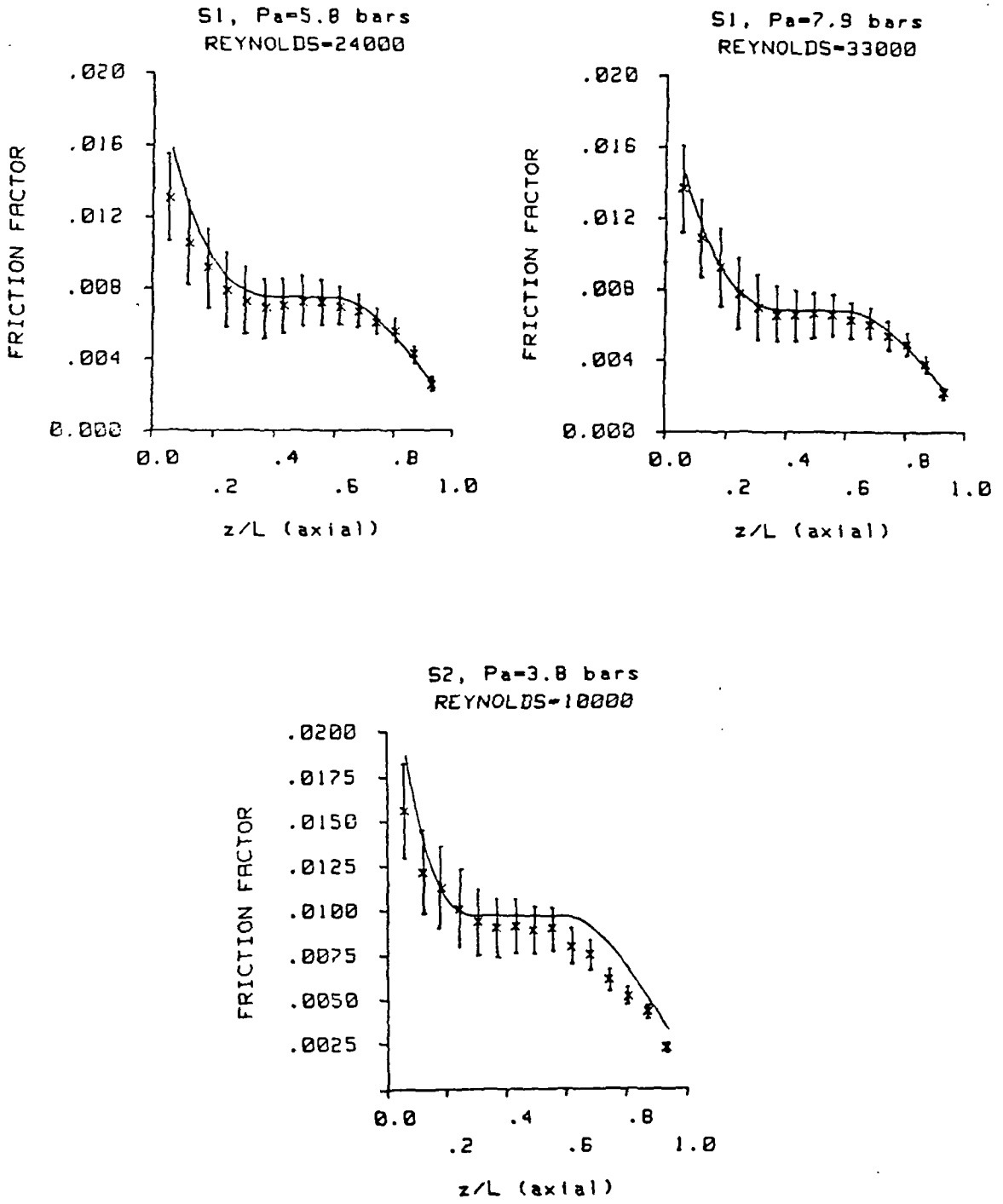

Figure 10. Empirical vs. experimental f_e for the smooth-stator seals of Table 1. Solid lines: empirical predictions.

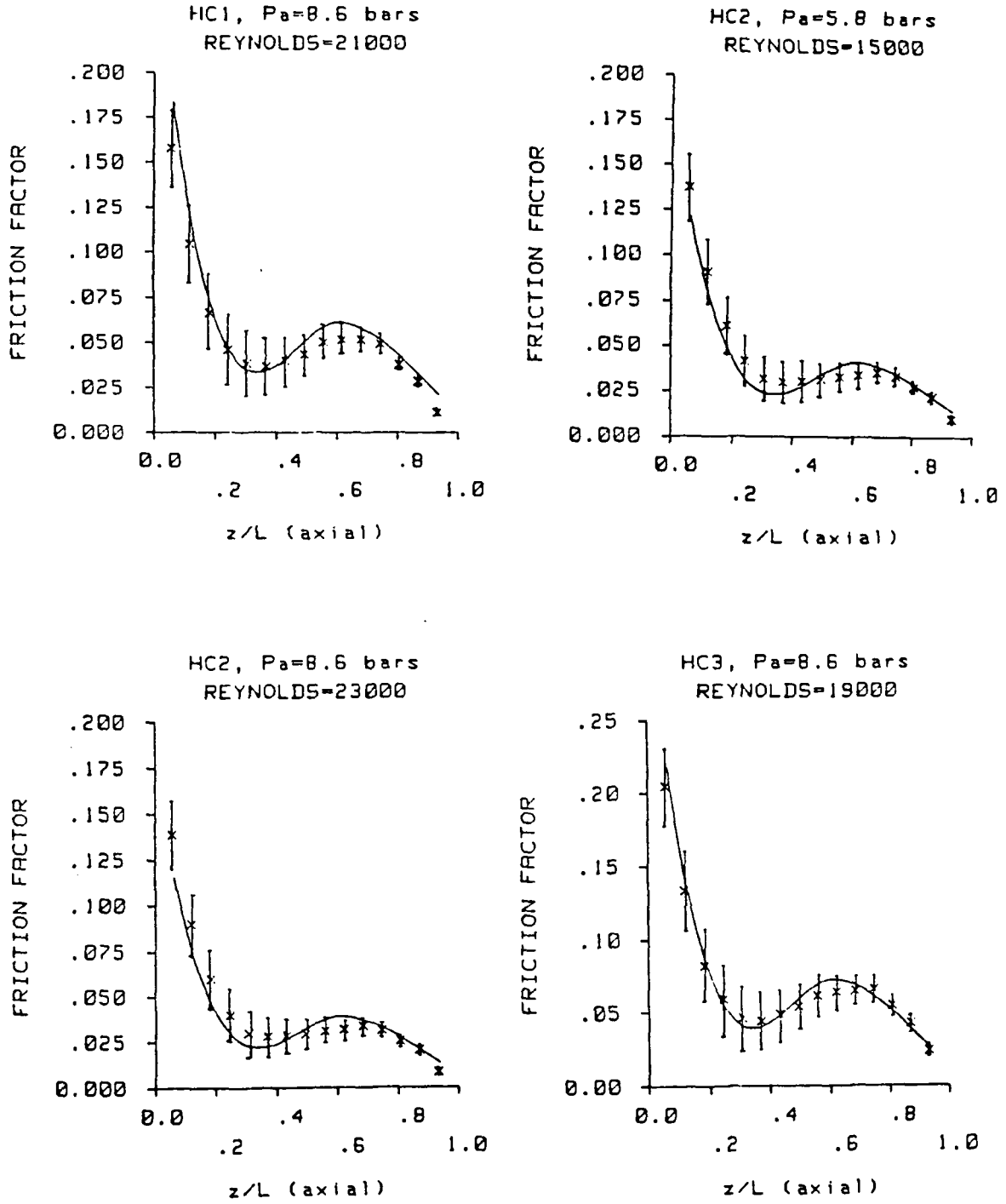

Figure 11. Empirical vs. experimental f_e for the honeycomb-stator seals of Table 1. Solid lines: empirical predictions.

defined by equations (50), (52) through (56), (58), and (60). The experimental results show that f_e is high near the inlet of the honeycomb-stator seals, which disagrees with the friction factor model used in the flat-plate-flow analysis.

First-Order Perturbations

For the empirical friction factor model above, the first-order perturbations of equations (52) and (53) in terms of the variables defined in equation (4) are

$$f_{s1} = f_{s0}\left(\frac{\Psi_{ds1}}{\Psi_{ds0}} + \frac{\Psi_{x1}}{\Psi_{x0}} + \frac{f_{Bs1}}{f_{Bs0}}\right) \tag{61}$$

and

$$f_{r1} = f_{r0}\left(\frac{\Psi_{dr1}}{\Psi_{dr0}} + \frac{\Psi_{x1}}{\Psi_{x0}} + \frac{f_{Br1}}{f_{Br0}}\right) \quad . \tag{62}$$

Since Ψ_{x0} is independent of the perturbation variables, $\Psi_{x1} = 0$. Similarly, $\Psi_{ds1} = 0$ for a honeycomb stator. For a smooth stator,

$$\Psi_{ds1} = \psi_s\left[\frac{x_{s1}}{x_{s0}} - \frac{H_1}{H_0}\right]$$

for $x_{s0}/L_e < 1.0$, where

$$\psi_s = -5.16(x_{s0}/L_e) + 10.08(x_{s0}/L_e)^2 - 4.92(x_{s0}/L_e)^3 \quad .$$

and x_{s1} is defined by equation (34). For $x_{s0} \geq 1.0$, $\Psi_{ds1} = 0$. Ψ_{dr1} is expressed similarly. Finally,

$$f_{Bs1} = f_{Bs0}mo_s\left[\frac{\rho_1}{\rho_0} + \frac{H_1}{H_0} + \frac{U_{\theta 0}U_{\theta 1} + U_{z0}U_{z1}}{U_{\theta 0}^2 + U_{z0}^2}\right] \quad ,$$

and

$$f_{Br1} = f_{Br0}mo_r\left[\frac{\rho_1}{\rho_0} + \frac{H_1}{H_0} + \frac{(U_{\theta 0} - R\omega)U_{\theta 1} + U_{z0}U_{z1}}{(U_{\theta 0} - R\omega)^2 + U_{z0}^2}\right] \quad .$$

CHAPTER VII

STATIC PRESSURE AND LEAKAGE RESULTS

The test apparatus described in Chapter IV has been used for stationary-rotor tests of six seals. Three smooth-stator/smooth-rotor seals (S1, S2, and S3 in Table 1) and three honeycomb-stator/smooth-rotor seals (HC1, HC2, and HC3 in Table 1) have been tested, with no prerotation of the inlet air. Stationary-rotor tests were conducted at nine inlet pressures: from 3.08 bars to 8.60 bars, in 0.69 bar increments. Seals S1, HC1, HC2, and HC3 of Table 1 have also been tested dynamically; the dynamic test conditions are described in Chapter IV.

In this chapter, experimental leakage and pressure gradient results are compared to the predictions of three gas seal analyses. *In the figures in this chapter, curves 1, 2, and 3 represent the predictions of the fully-developed-flow, flat-plate-flow, and empirical-friction-factor analyses, respectively. Experimental results are designated by the letter "x".* The experimental results have been reported by Elrod and Childs (1988).

Leakage

All three analyses predict leakage well, especially for the honeycomb seals. Typical plots of predicted and experimental leakage for the test seals are shown in figure 12. The results shown are from dynamic tests of seals S1 and HC2 of Table 1. The uncertainty in the experimental results is about 1%. In the plot for seal S1, the circumferential velocity ratio is the ratio of the circumferential velocity of the air upstream of the seal to the rotor surface speed ($U_{\theta a}/R\omega$). The empirical-friction-factor analysis predicts lower leakage values than the fully-developed-flow and flat-plate-flow analyses because the friction factor in the entrance region of the seal is much higher for the empirical-friction-factor analysis.

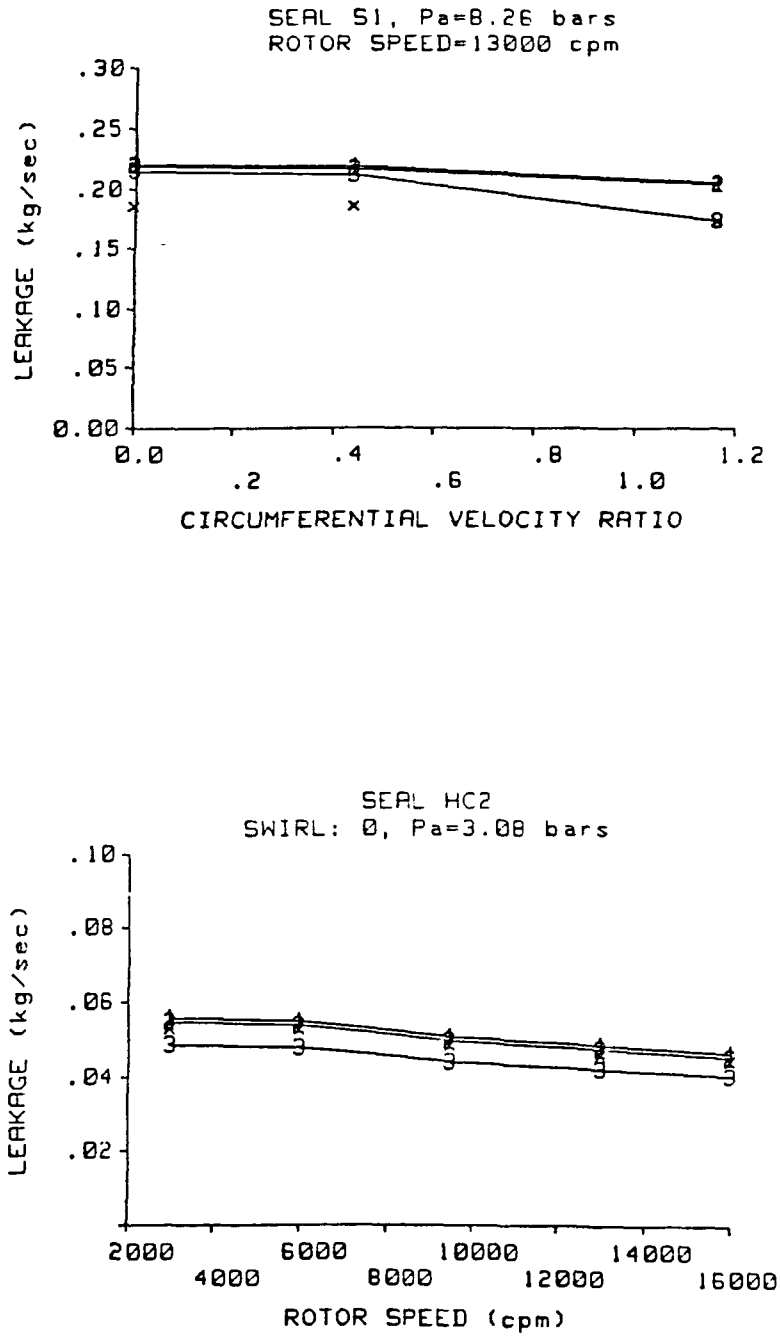

Figure 12. Leakage results for dynamic tests of seals S1 and HC2 of Table 1.

Pressure Gradient

Experimental and predicted pressure gradients are shown in figure 13. The results shown are from dynamic tests of seals S1 and HC2 of Table 1. Both test cases shown in the figure are choked flow cases. P/Pa is the dimensionless seal pressure, and z/L is the dimensionsless axial location. The uncertainty in the dimensionless pressures is less than 0.05. In each test case, there is little difference between the pressure gradients predicted by the fully-developed-flow and flat-plate-flow analyses. The flat-plate-flow and empirical-friction-factor analyses predict a steeper slope for the pressure gradient at the seal inlet ($z/L < 0.1$) than the fully-developed-flow analysis, because the difference between the friction factors of the flat-plate-flow and empirical-friction-factor analyses and the friction factor used in the fully-developed-flow analysis is greatest at the seal inlet.

Generally, the empirical-friction-factor analysis predicts the pressure gradient better than the fully-developed-flow and flat-plate-flow analyses, especially in the exit region ($z/L > 0.6$) of the seals. The pressure drop in the last 10% to 25% of the seal length is overpredicted by the fully-developed-flow and flat-plate-flow analyses. For seal HC2, the pressure gradient predicted by the empirical-friction-factor analysis for $z/L < 0.4$ indicates a need for further investigation of the friction factor characteristics of honeycomb surfaces.

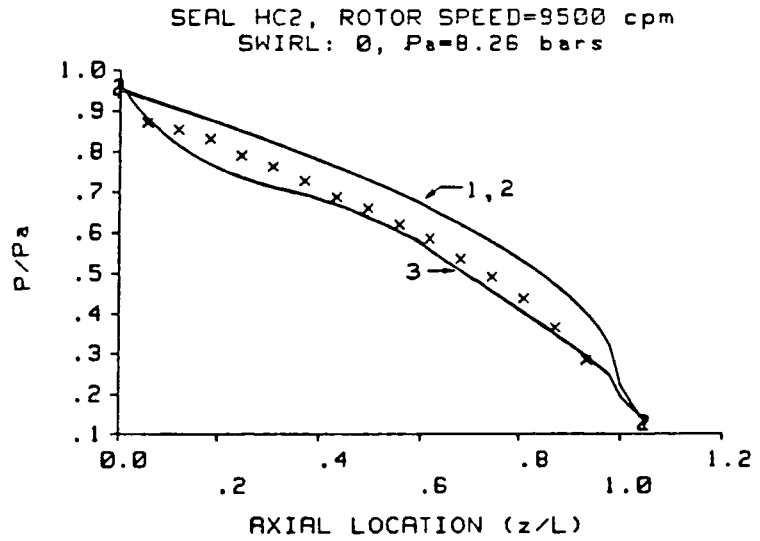

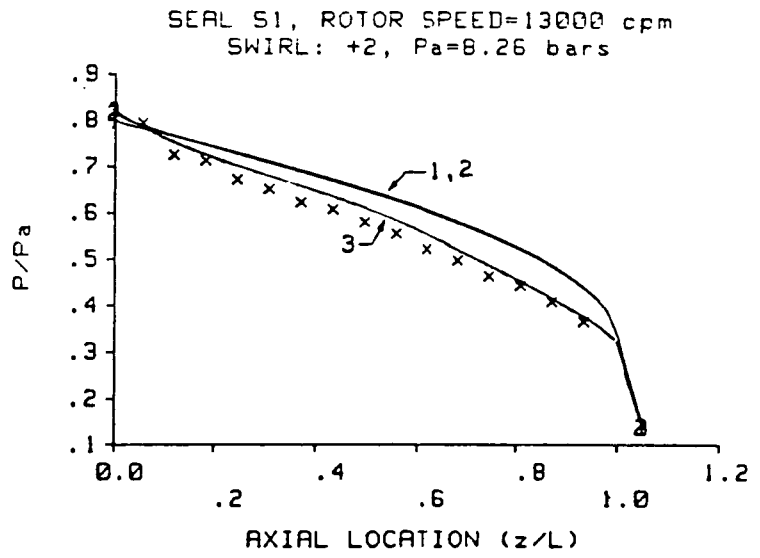

Figure 13. Pressure gradients for dynamic tests of seals HC2 and S1 of Table 1.

CHAPTER VIII

DYNAMIC TEST RESULTS

The air-seal apparatus described in Chapter IV has been used to test smooth-stator/smooth-rotor seals with constant and tapered stator diameters, honeycomb-stator seals with smooth and labyrinth rotors, labyrinth-stator/smooth-rotor seals, smooth-stator/labyrinth-rotor seals, and a seal with interlocking stator and rotor. In this chapter, rotordynamic coefficient results from tests of one smooth-stator/smooth-rotor seal (S1 in Table 1, Chapter IV) and three honeycomb-stator/smooth-rotor seals (HC1, HC2, and HC3 in Table 1) are compared to the predictions of three gas seal analyses. The predicted dependencies of rotordynamic coefficients on rotor speed (ω), inlet circumferential velocity ratio ($u_{\theta a} = U_{\theta a}/R\omega$), and seal inlet-to-exit pressure ratio ($Pr = p_a/p_b$) are compared to experimental results.

As described in Chapter I and illustrated in figure 1, the stability of a seal in which the rotor is whirling at a frequency ω depends on the cross-coupled stiffness and direct damping (k and C, respectively) of the seal. Cross-coupled stiffness depends on the magnitude and direction (with respect to rotor rotation) of U_θ. In the following paragraphs, comparisons of the experimental and predicted dependencies of k and C on ω, $u_{\theta a}$, and Pr are emphasized. Comparisons for the direct stiffness, K, are also presented.

For the rotor-speed dependence of the rotordynamic coefficients, results are shown for $u_{\theta a} = 0$ (swirl case 0 of Table 2). For any other swirl case, the inlet circumferential velocity ratio $u_{\theta a}$ decreases by about 80% when the rotor speed is increased from 3000 cpm to 16000 cpm. For the dependence of the rotordynamic coefficients on the inlet circumferential velocity ratio, results are shown for $0 \leq$

$u_{\theta a} < 1.2$. For the dependence of the rotordynamic coefficients on Pr, results are shown for $u_{\theta a} \approx 1.0$, a typical value of $u_{\theta a}$ in practice. *In the figures in this chapter, curves 1, 2, and 3 represent the predictions of the fully-developed-flow, flat-plate-flow, and empirical-friction-factor analyses, respectively. Experimental results are designated by the letter "x".* The experimental results have been reported by Elrod and Childs (1988).

Relative Uncertainty

The uncertainty in the dynamic coefficients can be determined using the method described by Holman (1978). The uncertainty in the force, excitation frequency, and displacement measurements are 0.44 N (0.1 lb), 0.065 Hz, and 0.0013 mm (0.05 mils), respectively. The maximum calculated uncertainties in the stiffness and damping coefficients for seals S1, HC1, HC2, and HC3 are given in Table 5.

Table 5. Maximum Uncertainties.

Seal	k	C	K
S1	31.2 N/mm	0.044 N-s/mm	20.4 N/mm
HC1	6.5 N/mm	0.036 N-s/mm	16.9 N/mm
HC2	9.0 N/mm	0.050 N-s/mm	23.4 N/mm
HC3	9.4 N/mm	0.038 N-s/mm	18.0 N/mm

Direct Damping

All three seal analyses predict C well, especially for the honeycomb seals. For seal S1, predictions are generally within 30% of the experimental results. For the honeycomb seals, most predictions are within 20% of the experimental results. Among the analyses, there is little difference in the predicted dependence of C on $u_{\theta a}$ and Pr. Plots of C versus $u_{\theta a}$ and Pr are shown in figures 14-17. Plots of C versus rotor speed are shown in figures 18 and 19. For seal S1, there is no difference

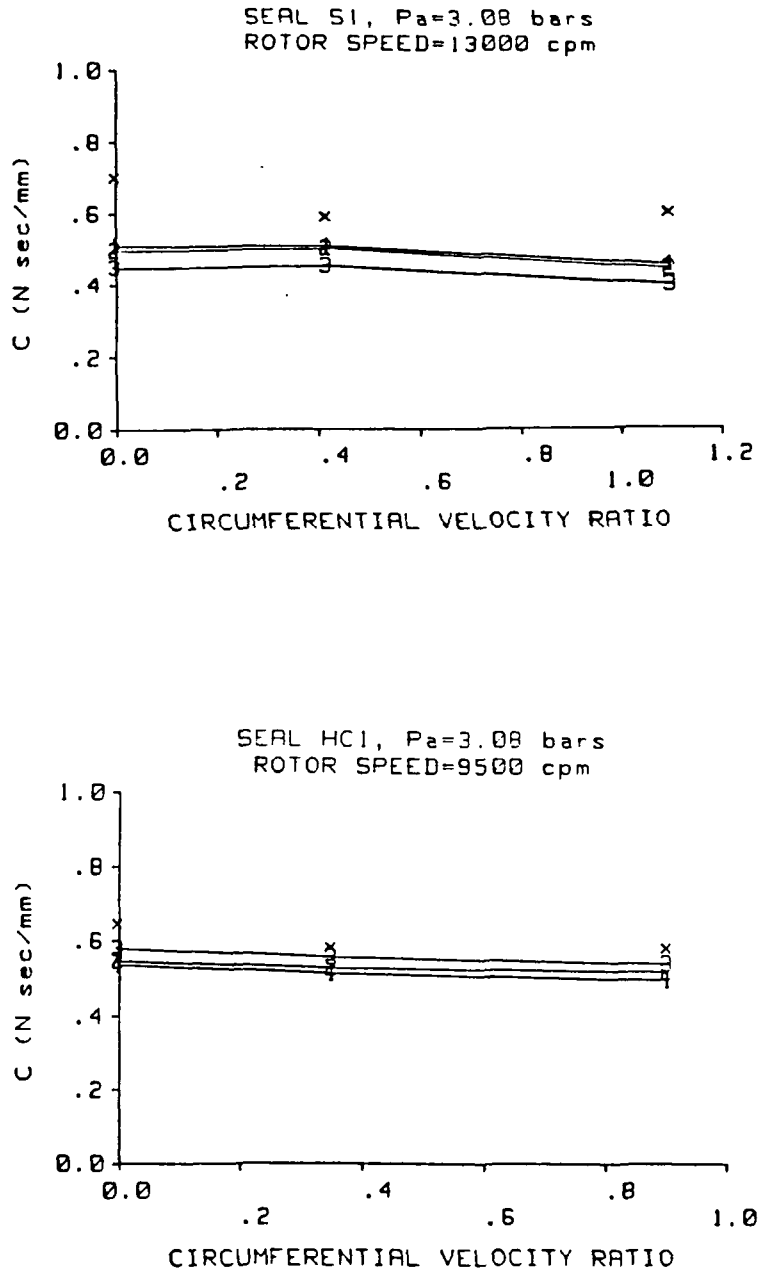

Figure 14. C **versus** $u_{\theta a}$ **for seals S1 and HC1 of Table 1.**

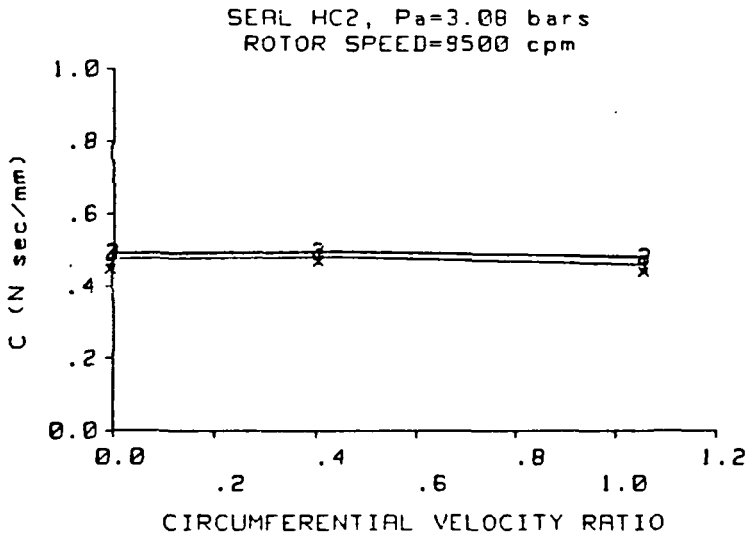

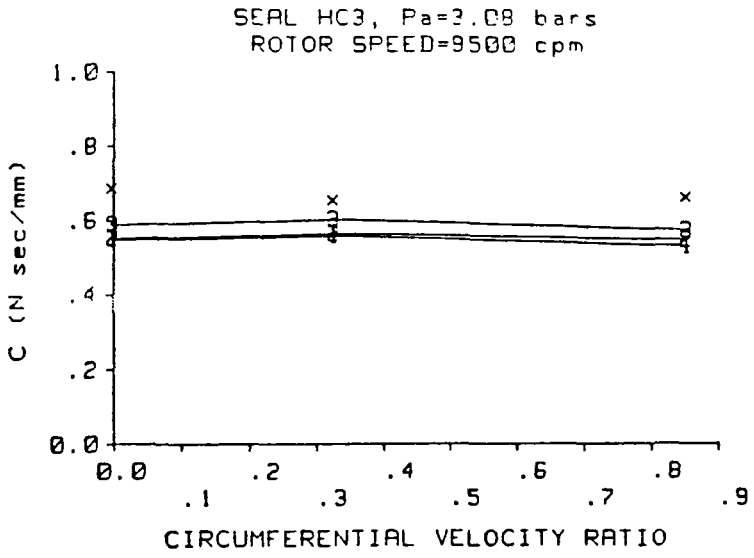

Figure 15. C **versus** $u_{\theta a}$ **for seals HC2 and HC3 of Table 1.**

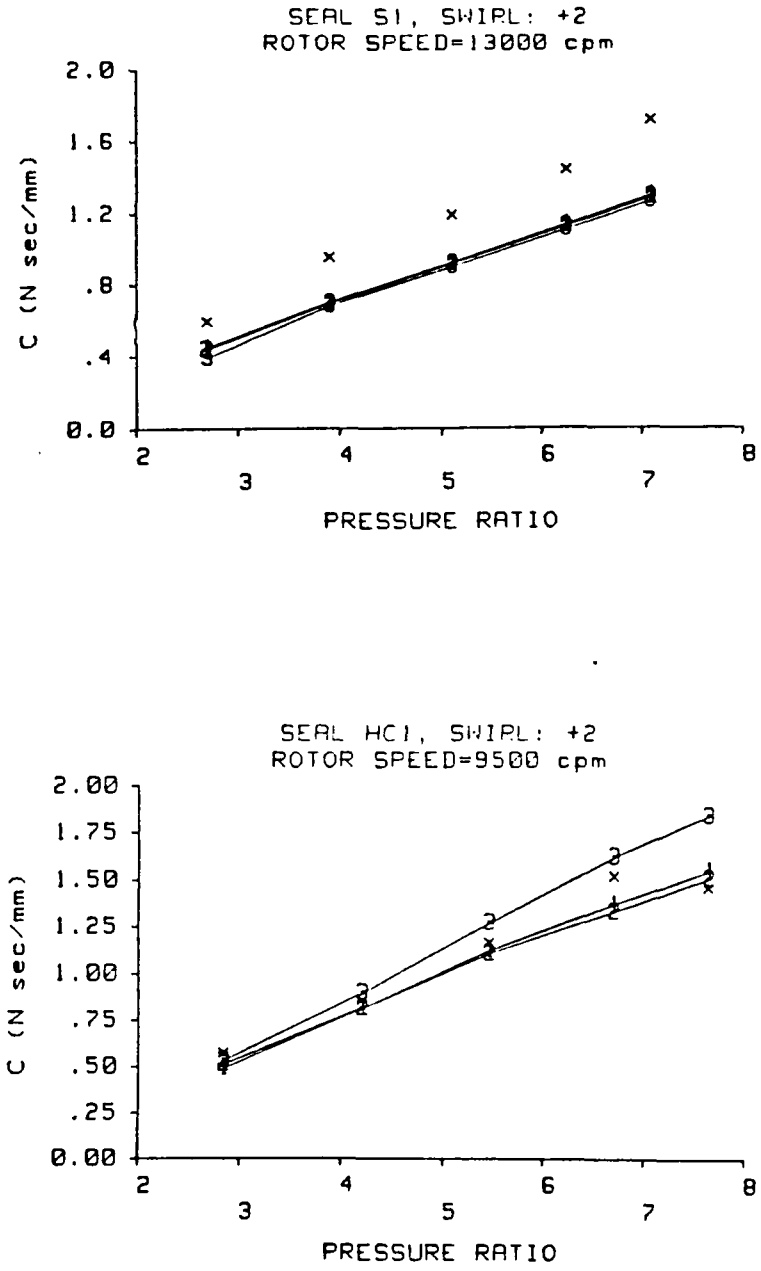

Figure 16. C **versus** P_r **for seals S1 and HC1 of Table 1.**

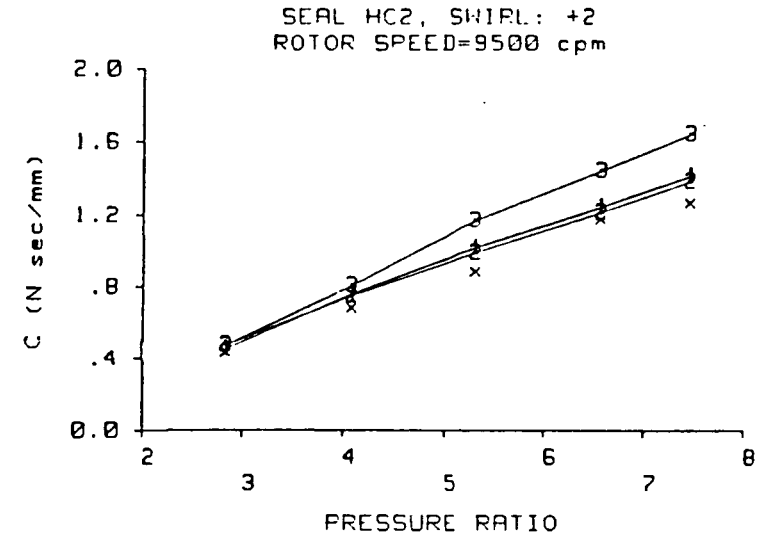

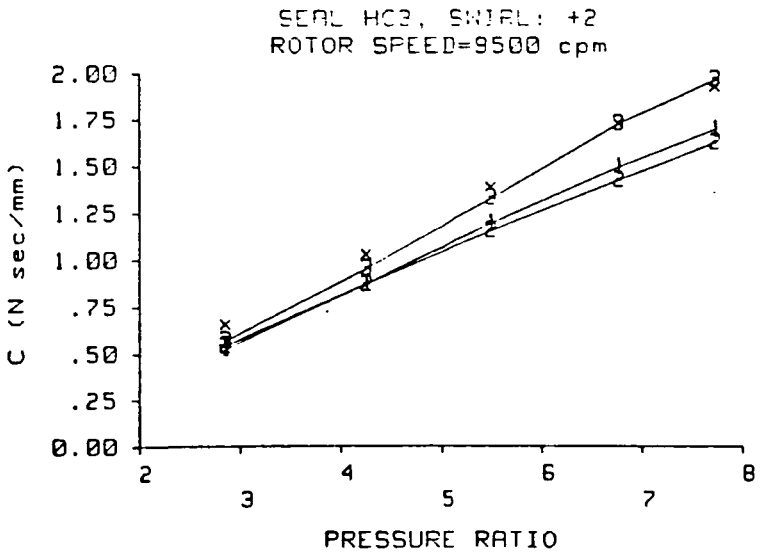

Figure 17. C versus P_r for seals HC2 and HC3 of Table 1.

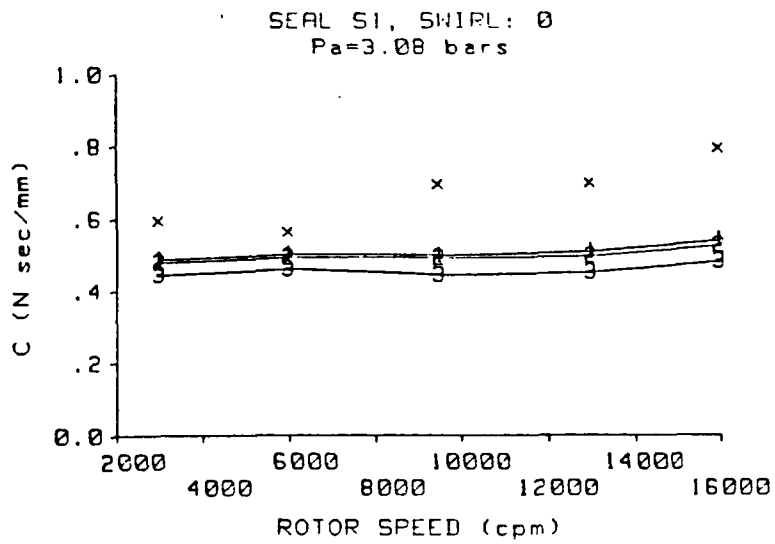

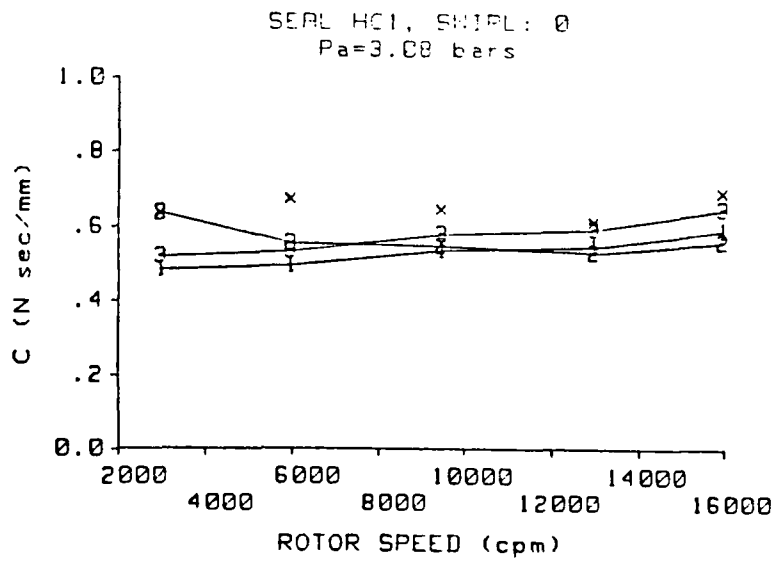

Figure 18. *C* **versus rotor speed for seals S1 and HC1 of Table 1.**

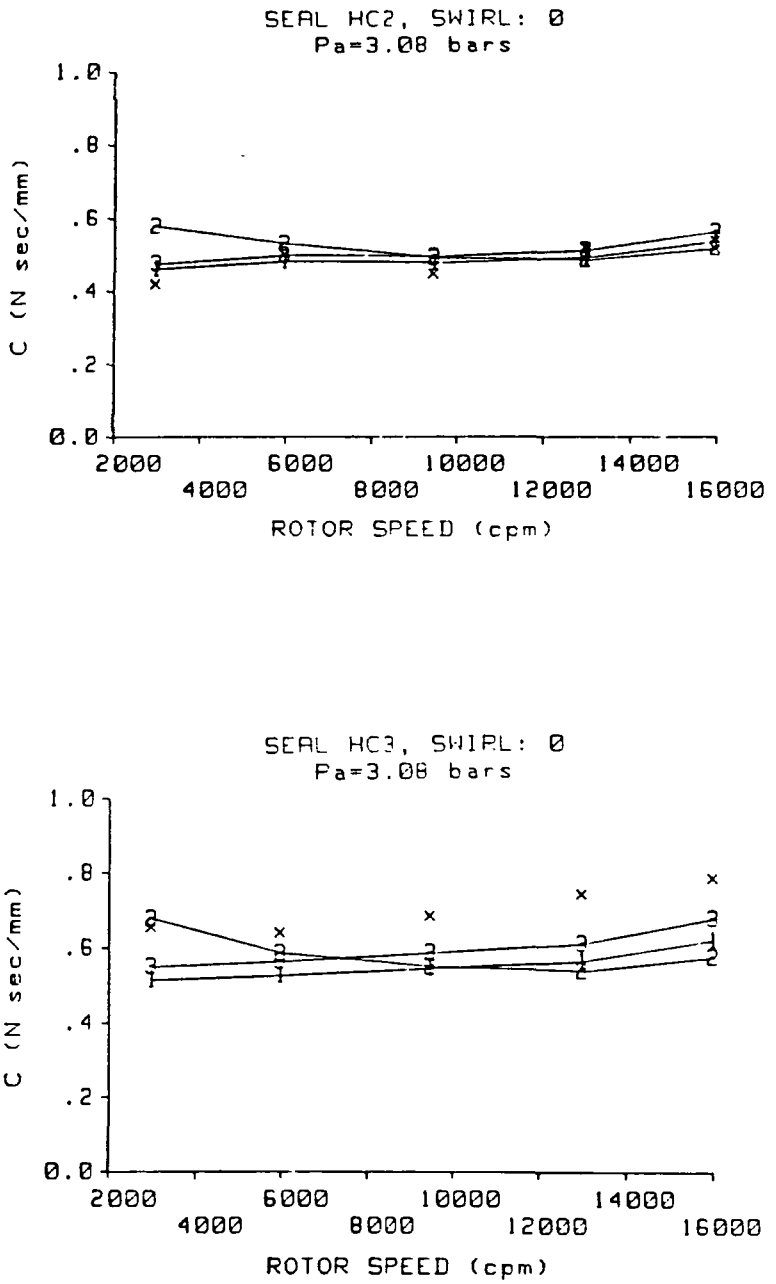

Figure 19. *C* versus rotor speed for seals HC2 and HC3 of Table 1.

in the predicted rotor speed dependence of C for the three analyses. The fully-developed-flow and empirical-friction-factor analyses predict that C increases as ω increases for all four test seals. For the honeycomb-stator seals, the flat-plate-flow analysis predicts that C decreases as the rotor speed is increased from 3000 cpm to about 13000 cpm, and then increases as rotor speed is further increased to 16000 cpm. In general, the rotor speed dependence of C is best predicted by the fully-developed-flow and empirical-friction-factor analyses.

Cross-Coupled Stiffness

Typical plots of k versus rotor speed are shown in figures 20 and 21. The negative experimental cross-coupled stiffnesses in the figures may be due to secondary flow patterns which are predicted by Tam et al. (1987) for smooth surfaces, low rotor speeds, and $U_{\theta a} \leq 0$, but are not modelled by bulk-flow analyses. For $k > 0$, the increase in k due to an increase in ω is best predicted by the flat-plate-flow and empirical-friction-factor analyses. Due to higher rotor drag in the entrance region, the predictions of the flat-plate-flow and empirical-friction-factor analyses are more speed dependent (i.e., $\Delta k/\Delta\omega$ is greater) than those of the fully-developed-flow analysis. There is generally little difference in the predicted dependence of k on ω for the flat-plate-flow and empirical-friction-factor analyses.

Figures 22 and 23 show the dependence of k on $u_{\theta a}$. The fully-developed-flow and flat-plate-flow analyses overpredict the increase in k due to an increase in $u_{\theta a}$, especially for the honeycomb seals. Because of the high f_s near the seal inlet, the empirical-friction-factor analysis predicts the increase in k due to an increase in $u_{\theta a}$ well.

For seals S1, HC1, HC2, and HC3, figures 24 and 25 show k versus Pr for $u_{\theta a} \approx 1.0$. For seals S1, HC1, and HC2, the empirical-friction-factor analysis predicts the dependence of k on Pr better than the fully-developed-flow and flat-

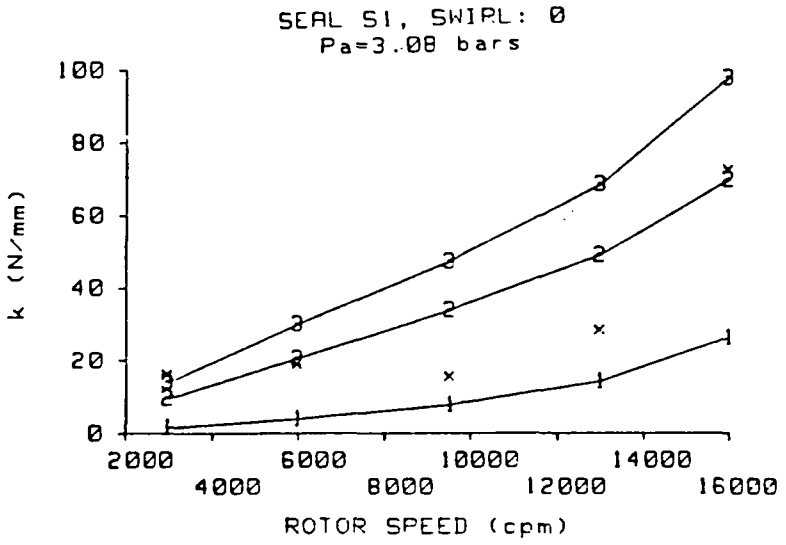

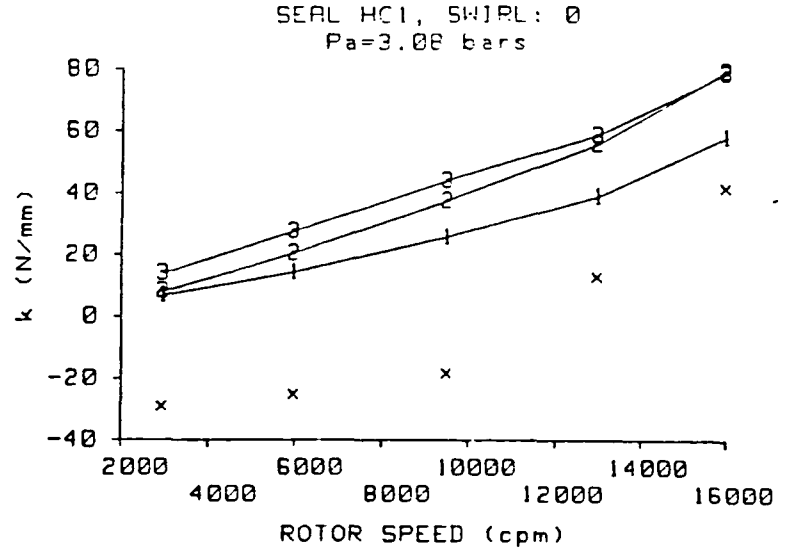

Figure 20. k versus rotor speed for seals S1 and HC1 of Table 1.

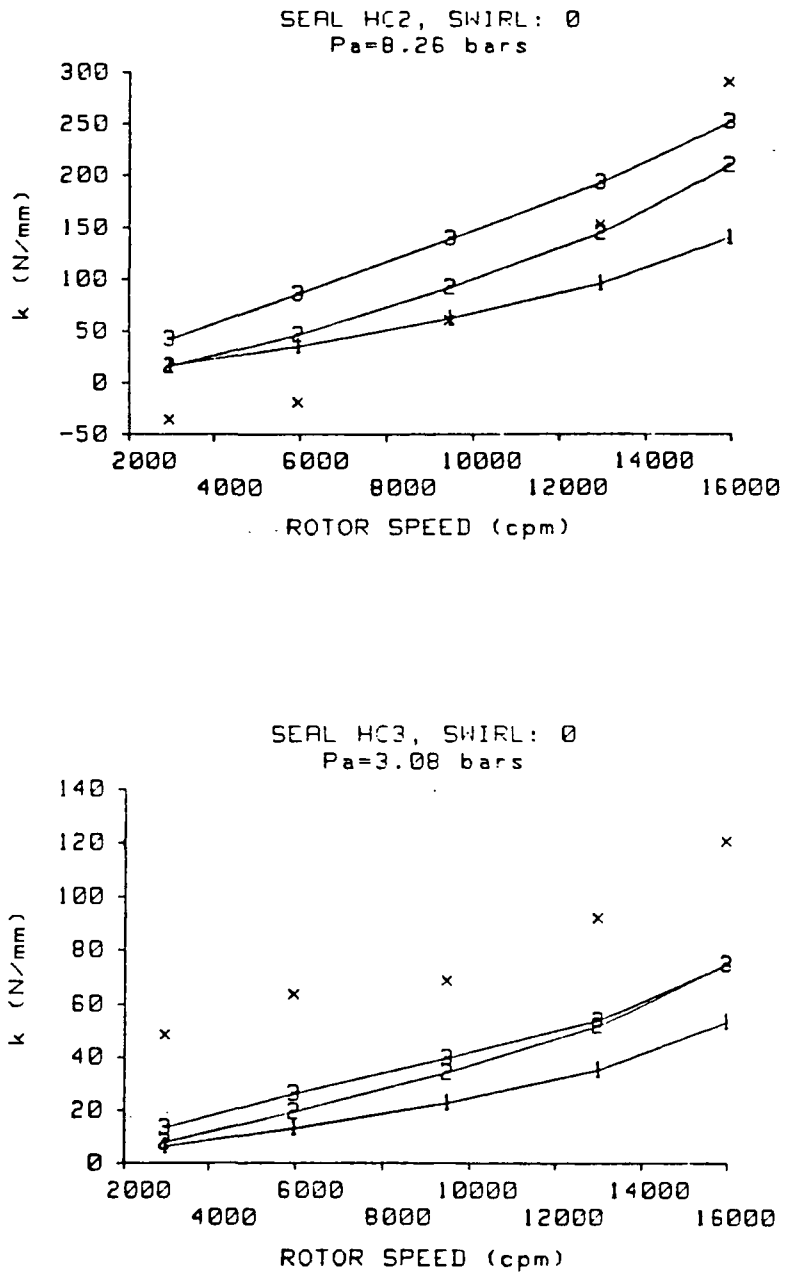

Figure 21. k versus rotor speed for seals HC2 and HC3 of Table 1.

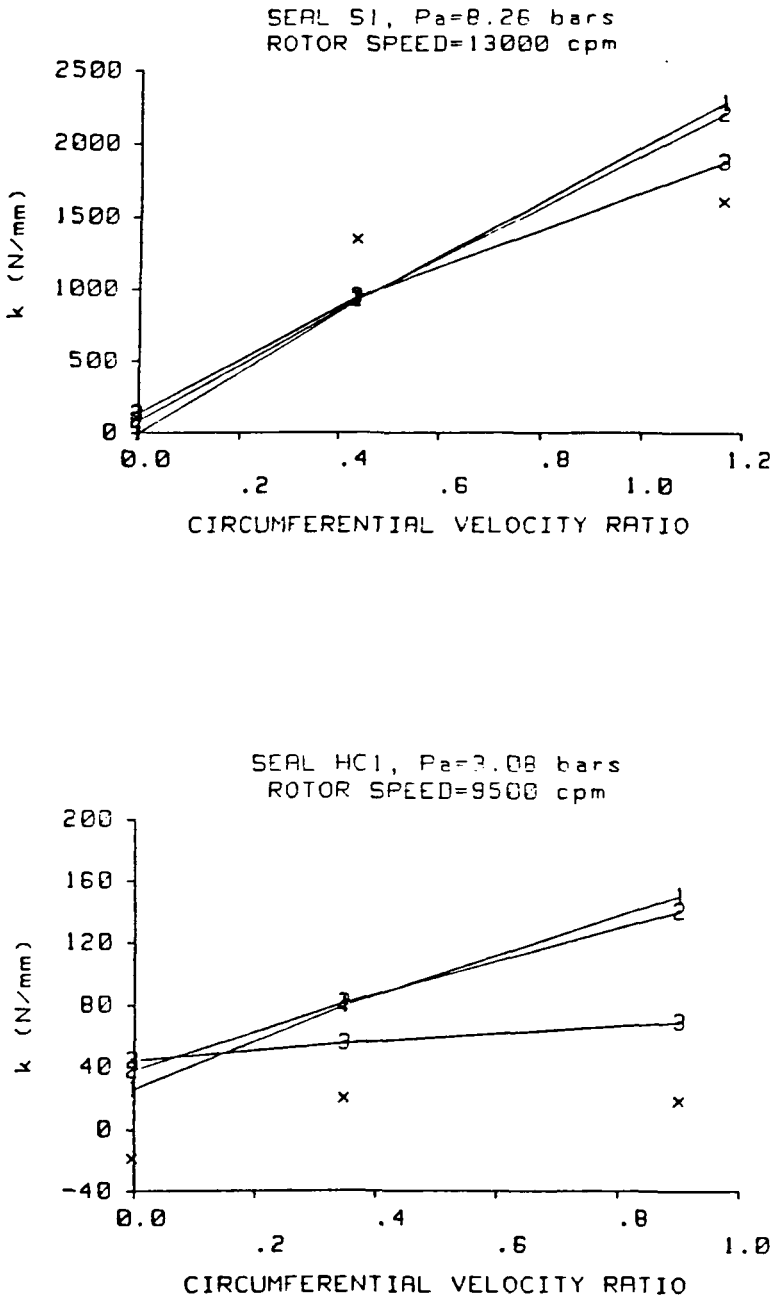

Figure 22. k versus $u_{\theta a}$ for seals S1 and HC1 of Table 1.

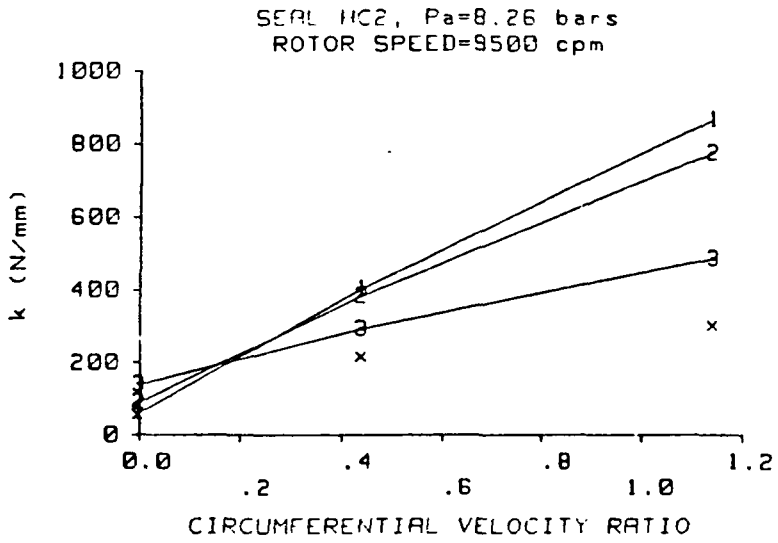

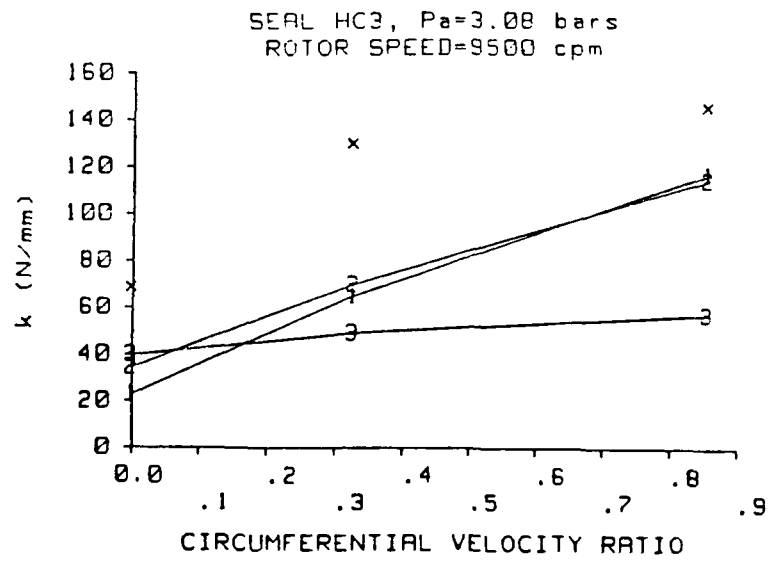

Figure 23. k **versus** $u_{\theta a}$ **for seals HC2 and HC3 of Table 1.**

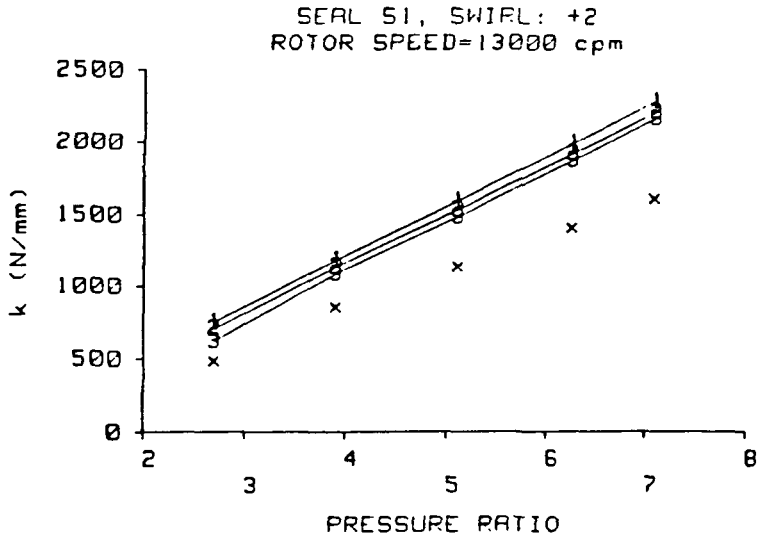

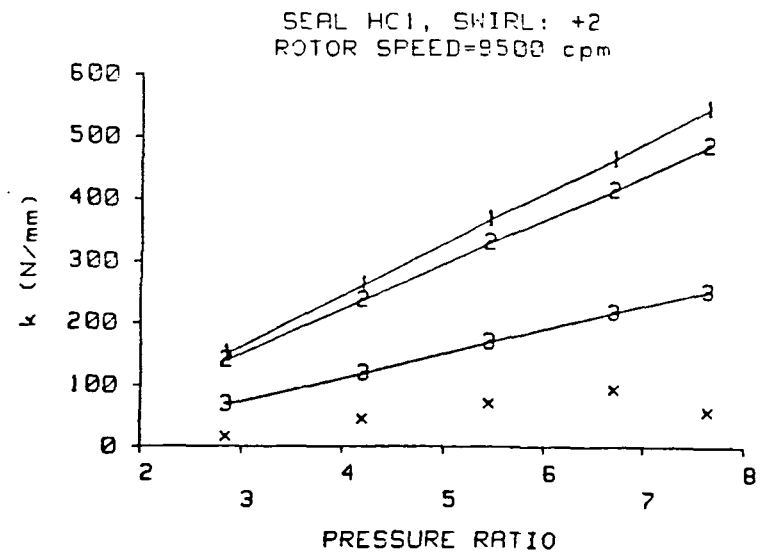

Figure 24. k versus P_r for seals S1 and HC1 of Table 1.

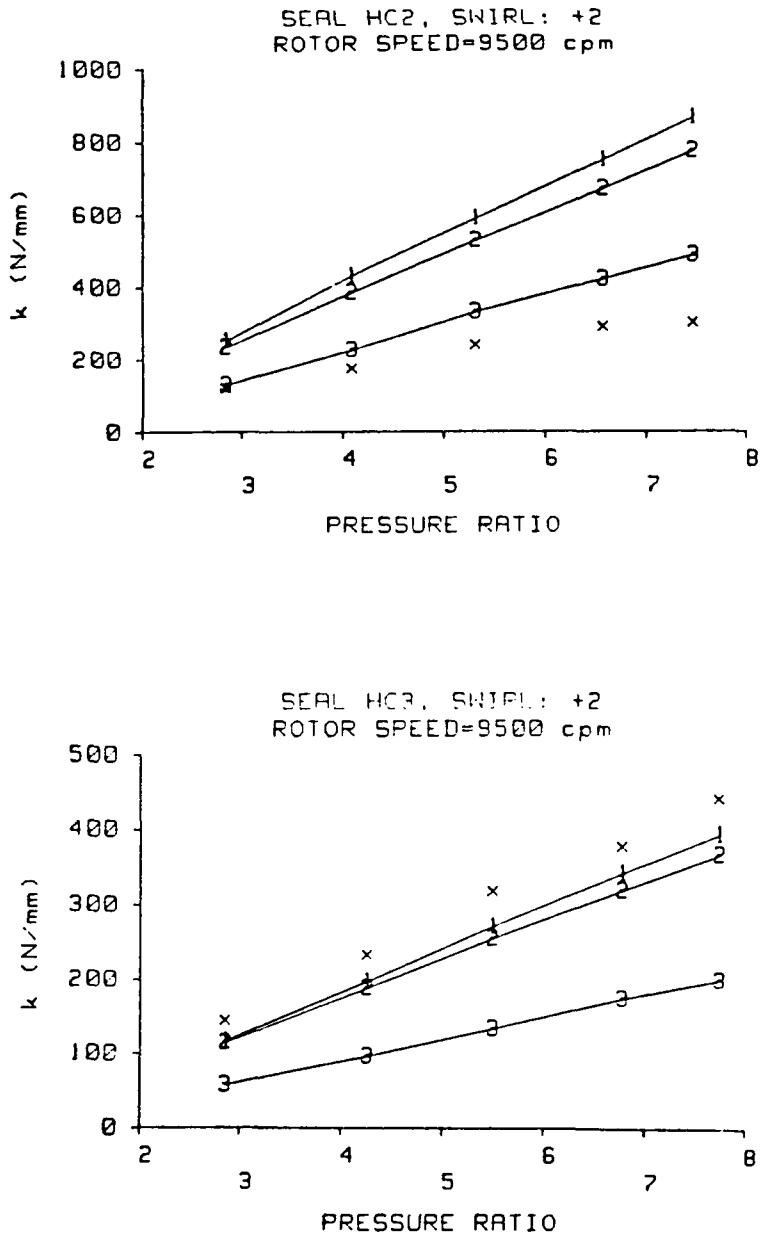

Figure 25. k versus P_r for seals HC2 and HC3 of Table 1.

plate-flow analyses. There is little difference between the predictions of the fully-developed-flow and flat-plate-flow analyses, and they predict the dependence of k on Pr for seal HC3 better than the empirical-friction-factor analysis.

Direct Stiffness

All three analyses predict K poorly, especially for the honeycomb seals. However, the direct stiffness of a gas seal normally affects turbomachinery rotordynamics less than k and C. Figures 26-31 show typical comparisons of predicted and experimental K for the test seals. A probable cause for the disagreement between experiment and analysis for the honeycomb seals is poor modeling of the honeycomb stator shear stresses. The friction factor characteristics of the honeycomb stators were obtained from tests of the seals at a clearance of 0.41 mm. The dependence of the friction characteristics of honeycomb surfaces on seal clearance has not been investigated.

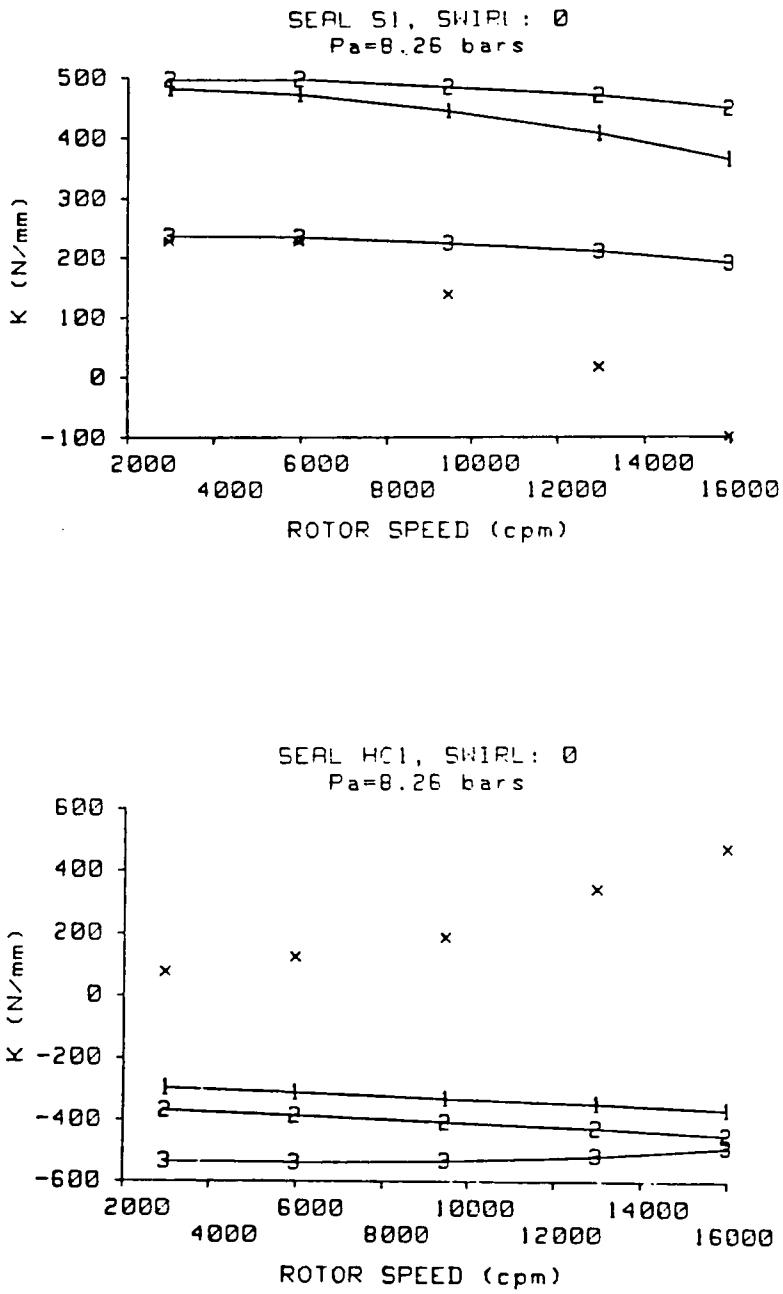

Figure 26. K versus rotor speed for seals S1 and HC1 of Table 1.

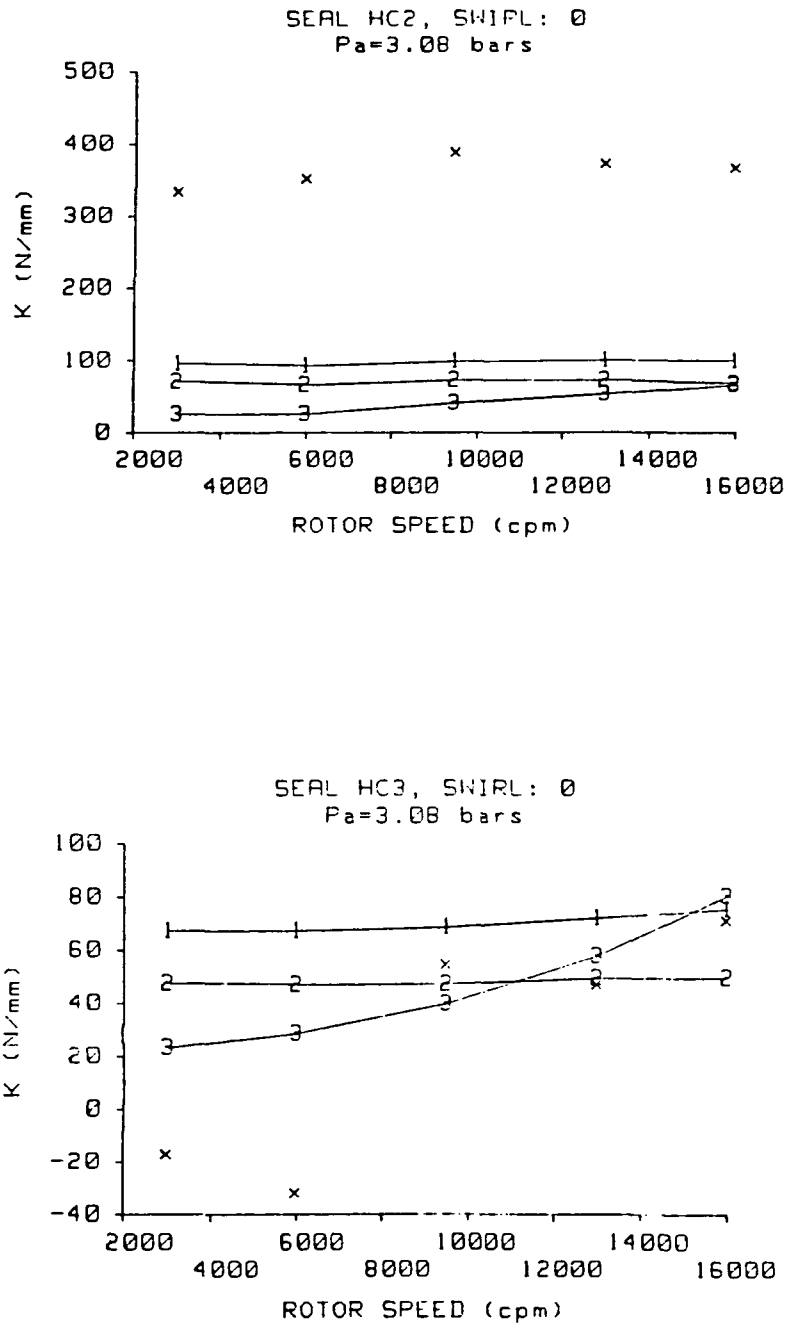

Figure 27. K versus rotor speed for seals HC2 and HC3 of Table 1.

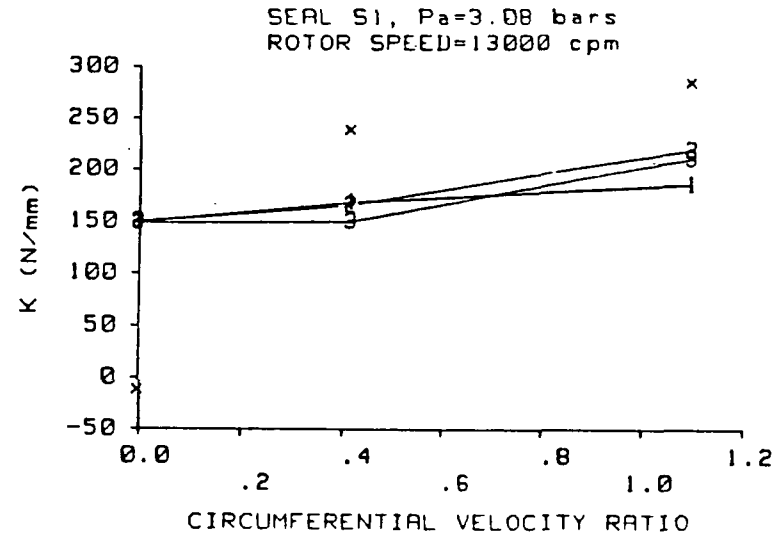

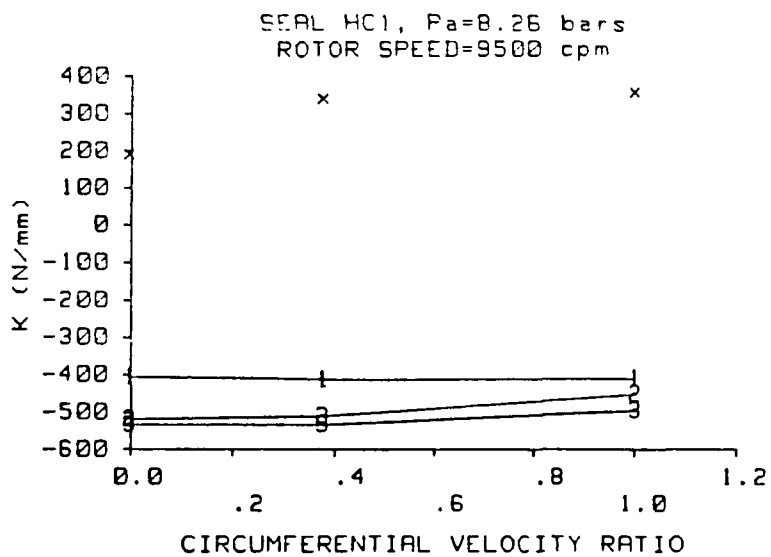

Figure 28. K versus $u_{\theta a}$ for seals S1 and HC1 of Table 1.

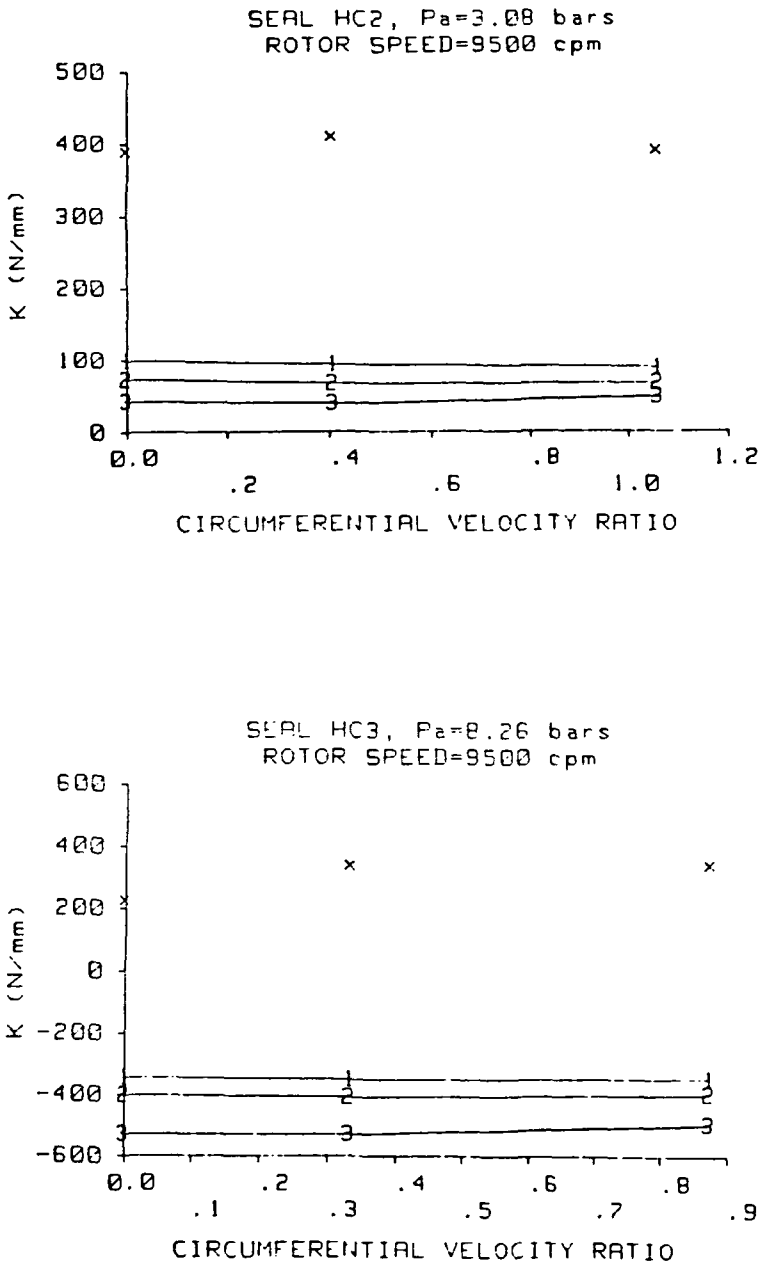

Figure 29. K versus $u_{\theta a}$ for seals HC2 and HC3 of Table 1.

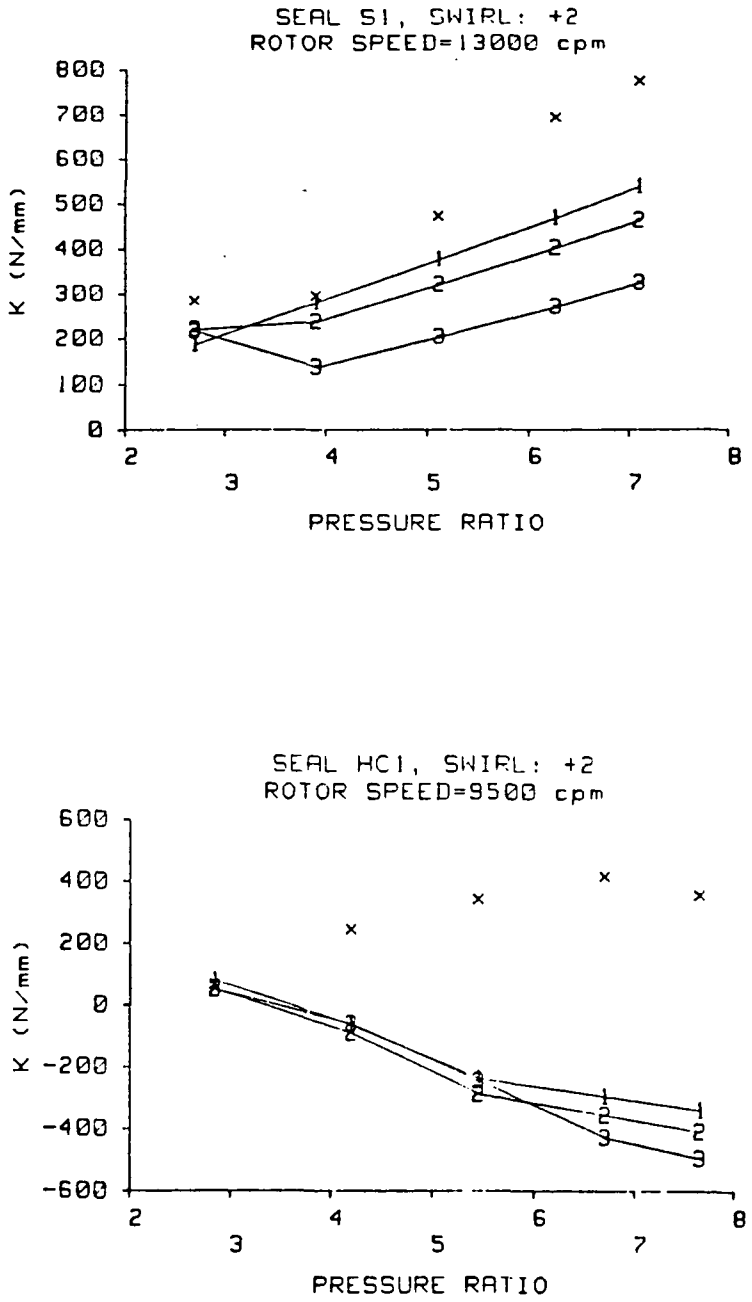

Figure 30. K versus P_r for seals S1 and HC1 of Table 1.

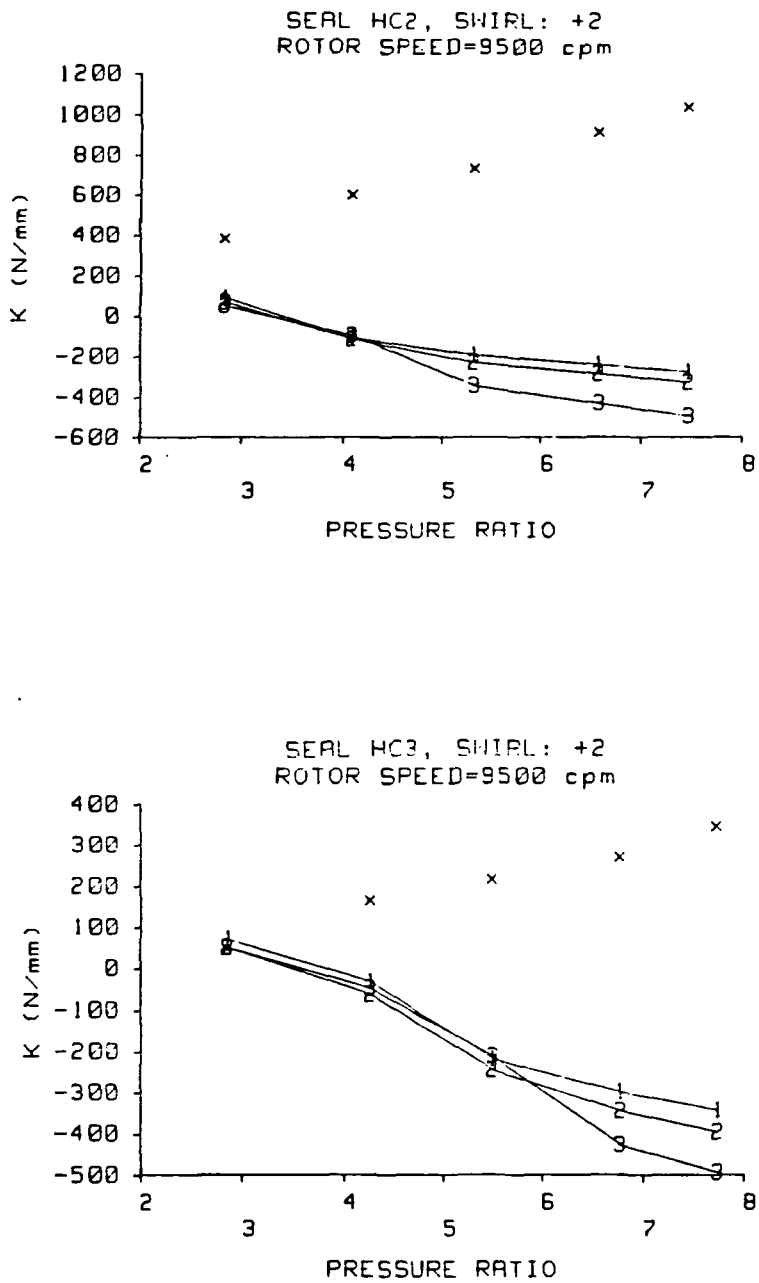

Figure 31. K versus P_r for seals HC2 and HC3 of Table 1.

CHAPTER IX

CONCLUSIONS

Nelson's (1984) rotordynamic analysis for centered, annular gas seals has been revised by including the fluid circumferential velocity in the Mach number definition. Two friction factor models have been developed and used in annular seal analyses. In the flat-plate-flow model, the friction factor in the seal entrance region is based on flat plate flow theory. The empirical-friction-factor model uses empirical entrance region and exit region friction factors. A method for determining the friction characteristics of honeycomb stators has been described. The results from static and dynamic tests of seals with smooth rotors and smooth or honeycomb stators have been compared to the predictions of:

(a) a fully-developed-flow friction factor analysis;

(b) the flat-plate-flow analysis;

(c) the empirical-friction-factor analysis.

The comparisons in the preceding chapters support the following conclusions:

(a) Presently, only bulk-flow analyses can be used to predict the rotordynamic characteristics of honeycomb-stator seals. The three-dimensional flow analysis of Tam et al. (1987) provides a qualitative explanation for the inability of bulk-flow analyses to predict negative experimental k values for no fluid prerotation and low rotor speeds. However, the stator-wall boundary conditions assumed by Tam et al., and by Nordmann et al. (1987) in another three-dimensional seal analysis, make the use of their analyses questionable for modelling honeycomb-stator seals.

(b) For a bulk-flow annular gas seal analysis, cross-coupled stiffness predictions are significantly improved by accurate modelling of the wall shear stresses in the seal. Compared to the fully-developed-flow and flat-plate-flow analyses,

the empirical-friction-factor analysis predicts k best for annular gas seals. Experimental rotor surface speeds are lower than those in many seal applications, so the improved ability of the flat-plate-flow and empirical-friction-factor analyses to predict rotor speed dependence is attractive. Since the inlet circumferential velocity ratio ($u_{\theta a}$) is between 0.5 and 1.0 in many seal applications, the improved ability of the empirical-friction-factor analysis to predict the dependence of k on $u_{\theta a}$ is especially attractive.

(c) Since the friction factor is high for a flow distance of about fifty seal clearances, the importance of using an entrance-region shear-stress model, instead of an abrupt entrance-loss, increases as the ratio of seal-clearance to seal-length (H/L) increases.

(d) The fully-developed-flow and flat-plate-flow analyses overpredict the pressure loss in the last 10% to 25% of a seal. Generally, the fully-developed-flow and flat-plate-flow analyses underpredict the pressure loss at the seal inlet. The empirical-friction-factor analysis, with an exit region friction factor and a higher entrance region friction factor than the other two analyses, predicts seal pressure gradients well. The dependence on seal length and clearance of the empirical friction factor model developed in Chapter VI should be investigated further.

(e) Further experimental investigation of the entrance-region shear stresses in seals would improve the present entrance-region friction model. The "forty-diameter rule" used in the flat-plate-flow and empirical-friction-factor analyses is based on the experimental results of Keenan and Neumann (1946) and Shapiro and Smith (1948), for which the minimum duct diameter was 9.5 mm. The results of Barbin and Jones (1963) and Wang and Tullis (1974) show that wall shear stress attains the fully developed flow value within fifteen diameters of the entrance of larger ducts (200 mm to 300 mm diameters). The experimental results of the

present study agree with those of Keenan and Neumann and Shapiro and Smith.

(f) The honeycomb-stator friction characteristics derived by the method described in chapter V have been used effectively for predicting static and dynamic characteristics of honeycomb-stator/smooth-rotor seals. Only the direct stiffness is predicted poorly by the empirical-friction-factor analysis. However, the method described in Chapter V does not model the dependence of the friction characteristics of honeycomb surfaces on seal clearance. Flat-plate tests of honeycomb surfaces which include variation of the clearance between the plates will provide an improved honeycomb shear-stress model. Implementation of flat-plate test results in the present seal analysis should improve predictions of the dynamic characteristics of honeycomb-stator/smooth-rotor seals.

(g) The entrance-region shear stress model used in the flat-plate-flow analysis is also applicable to incompressible seal analysis. The applicability to incompressible seal analysis of the friction model used in the empirical-friction-factor analysis must be determined experimentally.

(h) All three analyses predict K poorly. For gas seals, this coefficient generally does not have a major influence on rotordynamics.

REFERENCES

Allaire, P. E., Gunter, E. J., Lee, C. P., and Barrett, L. E., 1976, "The Dynamic Analysis of the Space Shuttle Main Engine High Pressure Fuel Turbopump Final Report, Part II, Load Capacity and Hybrid Coefficients for Turbulent Interstage Seals," University of Virginia Report UVA/528140/ME76/103.

Barbin, A. R., and Jones, J. B., 1963, "Turbulent Flow in the Inlet Region of a Smooth Pipe," *ASME Journal of Basic Engineering*, Vol. 85, No. 1, pp. 29-34.

Black, H. F., 1969, "Effects of Hydraulic Forces in Annular Pressure Seals on the Vibrations of Centrifugal Pump Rotors," *Journal of Mechanical Engineering Science*, Vol. 11, No. 2, pp. 206-213.

Black, H. F., and Jenssen, D. N., 1971, "Effects of High-Pressure Ring Seals on Pump Rotor Vibrations," ASME Paper No. 71-WA/FE-38.

Black, H. F., Allaire, P. E., and Barrett, L. E., 1981, "The Effect of Inlet Flow Swirl on the Dynamic Coefficients of High-Pressure Annular Clearance Seals," Ninth International Conference in Fluid Sealing, BHRA Fluid Engineering, Leeuwenhorst, The Netherlands.

Childs, D. W., 1983, "Finite-Length Solution for Rotordynamic Coefficients of Turbulent Annular Seals," *ASME Journal of Lubrication Technology*, Vol. 105, pp. 437-444.

Childs, D. W., 1984, "Finite-Length Solutions for the Rotordynamic Coefficients of Constant-Clearance and Convergent-Tapered Annular Seals," 3rd International Conference on Vibrations in Rotating Machinery, The Institution of Mechanical Engineers, York, England, Sept. 10-12.

Childs, D. W., 1987, "SSME Seal Test Program: Test Results for Smooth, Hole-Pattern, and Helically-Grooved Stators," Progress Report for NASA Marshall Space Flight Center Contract NAS8-35824 prepared by Texas A & M University, #TRC-Seal-7-87.

Childs, D. W., and Kim, C.-H., 1985, "Analysis and Testing for Rotordynamic Coefficients of Turbulent Annular Seals with Different Directionally-Homogenous Surface Roughness Treatments for Rotor and Stator Elements," *ASME Journal of Tribology*, Vol. 107, pp. 296-306.

Childs, D. W., Nelson, C. C., Nicks, C., Scharrer, J., Elrod, D., and Hale, K., 1986, "Theory Versus Experiment for the Rotordynamic Coefficients of Annular Gas Seals: Part 1–Test Facility and Apparatus", *Transactions of the ASME Journal of Tribology*, Vol. 108, pp. 426–432.

Childs, D. W., Elrod, D. A., Hale, R. K., 1988, "Rotordynamic Coefficient and Leakage Test Results for Interlock and Tooth-on-Stator Labyrinth Seals", ASME Paper No. 88-GT-87.

Deissler, R. G., 1953, "Analysis of Turbulent Heat Transfer and Flow in the Entrance Regions of Smooth Passages," NACA TN 3016.

Dietzen, F. J., and Nordmann, R., 1986, "Calculating Rotordynamic Coefficients of Seals by Finite-Difference Techniques," Proceedings from a workshop on Rotordynamic Instability Problems in High-Performance Turbomachinery–1986, held at Texas A&M University, College Station, TX, pp. 77-98.

Elrod, D. A., and Childs, D. W., 1988 "Experimental Rotordynamic Coefficient Results for Honeycomb Seals," Report No. TRC-Seal-1-88, Turbomachinery Laboratory, Texas A&M University, College Station, TX.

Fleming, D. P., 1978, "Stiffness of Straight and Tapered Annular Gas Seals," ASME Paper 78-Lub-18, ASME-ASLE Joint Lubrication Conference, Minneapolis, Minn.

Fleming, D. P., 1980, "Damping in Ring Seals for Compressible Fluids," NASA CP2133, Proceedings from a workshop on Rotordynamic Instability Problems in High-Performance Turbomachinery–1980, held at Texas A&M University, College Station, TX, pp. 169-188.

Hirs, G. G., 1973, "A Bulk-Flow Theory for Turbulence in Lubricant Films," *ASME Journal of Lubrication Technology*, April, pp. 137-146.

Holman, J. P., 1978, *Experimental Methods for Engineers*, McGraw-Hill, New York, NY, pg. 45.

Jenssen, D. N., 1970, "Dynamics of Rotor Systems Embodying High Pressure Ring Seals," Ph.D. dissertation, Heriot-Watt University, Edinburgh, Scotland.

John, J. E. A., 1984, *Gas Dynamics*, Allyn and Bacon, Newton, MA.

Keenan, J. H., and Neumann, E. P., 1946, "Measurements of Friction in a Pipe for Subsonic and Supersonic Flow of Air," *ASME Journal of Applied Mechanics*, Vol. 13, No. 2, p. A-91.

Lomakin, A. A., 1958, "Calculation of Critical Speed and Securing of Dynamic Stability of Hydraulic High-Pressure Pumps with Reference to the Forces Arising in the Gap Seals," *Energomashinostroenie*, Vol. 4, No. 1, pp. 1-5.

Massey, B. S., 1979, *Mechanics of Fluids*, 4th Ed., Van Nostrand Reinhold Co., New York.

Mullins, Z. C., and Barrett, L. E., 1983, "The Effects of Flow Development on the Dynamic Characteristics of Turbulent Flow Annular Seals," Report No. UVA/643092/MAE83/203, Rotating Machinery and Controls Industrial Research Program, the University of Virginia.

Nelson, C. C., 1984, "Analysis for Leakage and Rotordynamic Coefficients of Surface Roughened Tapered Annular Gas Seals," *ASME Journal of Engineering for Power*, Vol. 106, No. 4, pp. 927-934.

Nelson, C. C., 1985, "Rotordynamic Coefficients for Compressible Flow in Tapered Annular Seals," *ASME Journal of Tribology*, Vol. 107, No. 3, pp. 318-325.

Nelson, C. C., and Nguyen, D. T., 1987, "Comparison of Hirs' Equation With Moody's Equation for Determining Rotordynamic Coefficients of Annular Pressure Seals," *ASME Journal of Tribology*, Vol. 109, No. 1, pp. 144-148.

Nordmann, R., Dietzen, F. J., and Weiser, H. P., 1987, "Calculation of Rotordynamic Coefficients and Leakage for Annular Gas Seals by Means of Finite Difference Techniques," *ASME Rotating Machinery Dynamics*, Vol. 1, pp. 351-357.

Serghides, T. K., 1984, "Estimate Friction Factor Accurately," *Chemical Engineering*, Vol. 91, No. 5, pp. 63-64.

Shapiro, A. H., and Smith, R. D., 1948, "Friction Coefficients in the Inlet Length of Smooth Round Tubes," NACA TN 1785.

Tam, L. T., Przekwas, A. J., Muszynska, A., Hendricks, R. C., Braun, M. J., and Mullen, R. L., 1987, "Numerical and Analytical Study of Fluid Dynamic Forces in Seals and Bearings," *ASME Rotating Machinery Dynamics*, Vol. 1, pp. 359-370.

von Pragenau, G. L., 1982, "Damping Seals for Turbomachinery," NASA Technical Paper 1987.

Wang, J. S., and Tullis, J. P., 1974, "Turbulent Flow in the Entry Region of a Rough Pipe," *ASME Journal of Fluids Engineering*, Vol. 96, No. 1, pp. 62-68.

White, F. M., 1979, *Fluid Mechanics*, McGraw-Hill, New York, NY.

White, F. M., 1974, *Viscous Fluid Flow*, McGraw-Hill, New York, NY.

APPENDIX

Uncertainty in Friction Factors

The friction factor uncertainties were determined using the method described by Holman (1978). The uncertainty w_R in a result R which is a function of n primary measurements x_1 to x_n with uncertainties w_1 to w_n is

$$w_R = \left[\left(\frac{\partial R}{\partial x_1} w_1\right)^2 + \left(\frac{\partial R}{\partial x_2} w_2\right)^2 + \cdots + \left(\frac{\partial R}{\partial x_n} w_n\right)^2\right]^{1/2} .$$

The primary measurements in the friction factor calculations are seal clearance, pressure, flow rate, and stagnation temperature. The uncertainties in these measurements are about 13 μm, 0.0055 bars, 1%, and 0.6°K, respectively. As a result, the estimated uncertainty in the Mach number calculation is about 1%. Friction is high near the seal inlet, where dM/dz is small. Using equation (46), a small uncertainty in dM/dz causes a large uncertainty in the friction factor calculation when f_e is high and dM/dz is low. dM/dz is calculated using the curve fit of the experimental Mach numbers. For the smooth seals, the curve fit is within 1.5% of the experimental Mach numbers. For the honeycomb seals, the curve fit is within from 1% to 4% of the experimental Mach numbers.

Accuracy of mo and no

Figure A1 shows a comparison between average experimental friction factors (designated by the letter "x") and the friction factors predicted (solid line) using equation (2) and the friction coefficients in table 4. The error bands show the range of experimental values used in calculating the average friction factors.

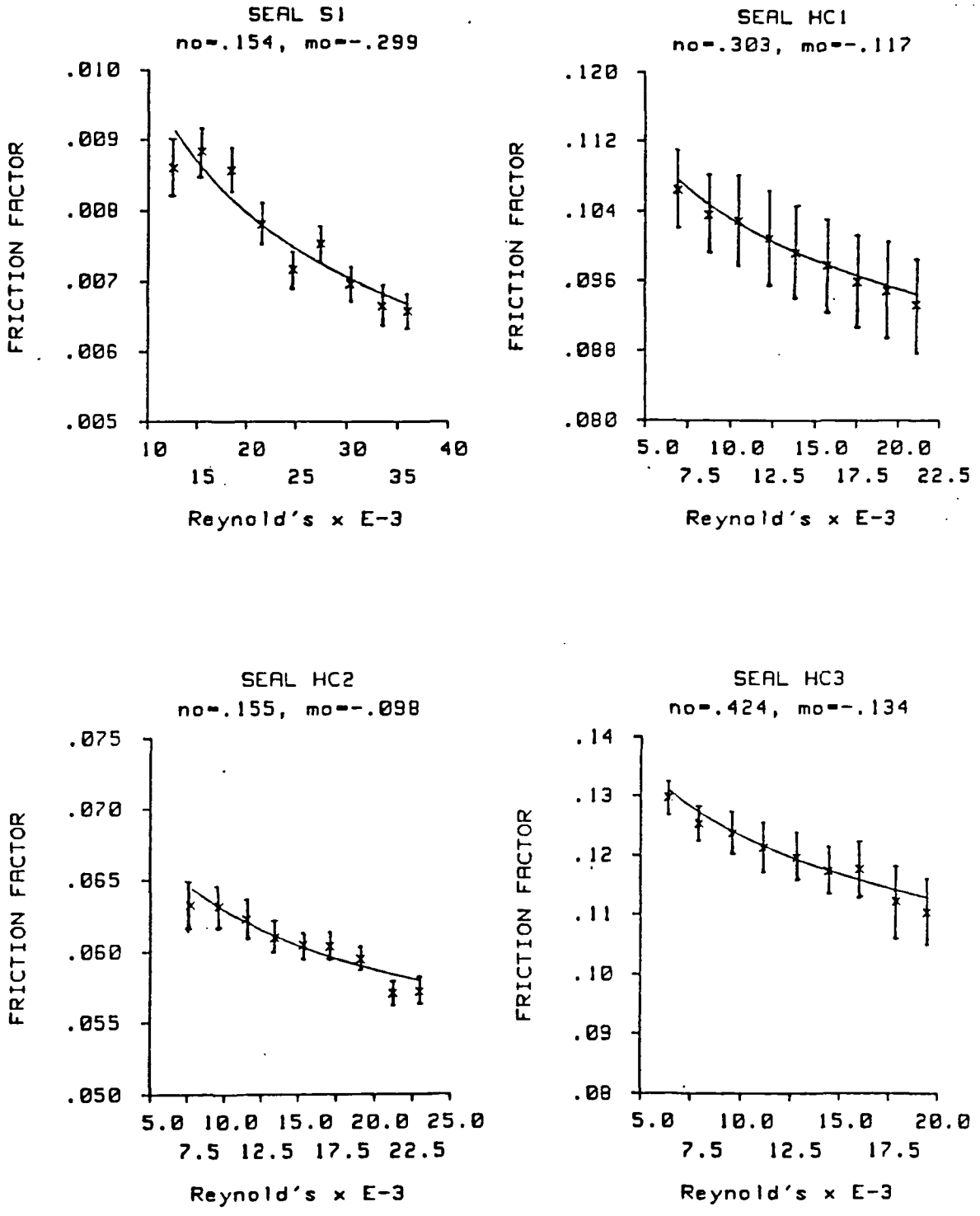

Figure A1. Friction factors versus Reynolds number. Solid lines: predictions using equation (2) and table 4.

VITA

David Alan Elrod received a B.S. Degree in engineering science from Louisiana State University in May of 1977. His work experience includes: one year with Brown & Root Company in Houston, Texas as a Quality Assurance Engineer in the Power Division; two and one-half years with Ashland Chemical Company in New Iberia, Louisiana as a maintenance engineer in a carbon black plant; and two and one-half years with Vulcan Materials Company in Geismar, Louisiana as a maintenance engineer in a chlor-alkali/chlorinated solvents facility. David enrolled as a graduate student at Texas A & M University in June of 1984, and received a M.S. Degree in mechanical engineering in December of 1986. His coursework and research has supported an interest in rotordynamics and vibrations. David's permanent mailing address is:

Mechanical Engineering Department
Virginia Polytechnic Institute and State University
Blacksburg, VA 24061.


TEXAS A&M UNIVERSITY
1876